Reverberation Mapping Analysis of the 2016 HST Campaign on NGC 4593

Lukas Diehl
George-August-Universität Göttingen

January 29, 2026

Abstract

Abstract

Contents

List of Figures

List of Tables

1. Introduction

Active galactic nuclei (AGNs) are among the most luminous objects in the universe, emitting radiation across the entire electromagnetic spectrum (Netzer 2013). Unlike inactive galaxies such as the Milky Way, the supermassive black hole (SMBH) in an active galaxy continues to accrete matter from its central region. This process generates thermal radiation (Peterson 1997) as well as non-thermal emission such as photoionization and subsequent recombination (Netzer 2013). AGN show strong variability across the entire electromagnetic spectrum, with timescales ranging from hours to days (Ulrich et al. 1997).
A particularly interesting example is the barred spiral galaxy NGC 4593. NGC 4593 shows strong variability from the X-ray to the optical bands (McHardy et al. 2017; Cackett et al. 2018) with several strong broad emission lines, including Balmer lines, Lyman lines and helium lines, among others (Kollatschny & Dietrich 1997; Cackett et al. 2018; Ochmann et al. 2025). Several studies have analysed the structure and kinematics of NGC 4593 (e.g. (Kollatschny & Dietrich 1997; Denney et al. 2006; Cackett et al. 2018)) using reverberation mapping (RM) of the broad emission lines. This method uses measurable time lags between the response of the emitting regions to variations in the ionizing continuum to probe the structure and size of the broad-line region (Peterson 1993).
In a recent work, Cackett et al. 2018 conducted an observation campaign using the Hubble Space Telescope (HST) with the Space Telescope Imaging Spectrograph (STIS), between 12 July and 6 August 2016 on NGC 4593, covering wavelength ranges from about 1100 Å to 1700 Å and from 3900 Å to 9000 Å. This work focused on the reverberation of the accretion disk of NGC 4593 by analyzing the UV and optical continua (Cackett et al. 2018). This dataset allows me to perform a classical reverberation mapping analysis of the broad emission-lines based on these data, and to determine the mass of the SMBH.
Furthermore, NGC 4593 shows strong emission in the O I λ8446 emission line and the Ca II λ8498 λ8542 λ8662 triplet (Ochmann et al. 2025). These low-ionization lines have not yet been included in RM campaigns yet. The O I λ8446 emission line is

particularly interesting, as it can get enhanced through Bowen fluorescence (Bowen 1947; Grandi 1980). Its presence allows the variability and time lag to be measured from a HST/STIS RM campaign for the first time.

2. Scientific Background

2.1 Active Galactic Nuclei

Active Galactic Nuclei (AGNs) refer to the central region of active galaxies. These objects are among the most luminous in the universe, with bolometric luminosities ranging from 10^{41} to 10^{48} erg s^{-1}, outshining entire galaxies by several orders of magnitude (Peterson 1997). Historically, several stellar-based models were proposed, such as dense star clusters or supermassive stars. However, these scenarios were discarded, as they are expected to collapse into black holes themselves, and they cannot provide the required energy output. Today, it is understood that the enormous luminosities of AGN are powered by accretion of matter onto a supermassive black hole (SMBH) at the centers of galaxies (Rees 1984). The most widely accepted model for this accretion is a hot, rotating accretion disk surrounding the SMBH, which produces most of the observed radiation (Shakura & Sunyaev 1973). The following sections will outline the key components of an AGN and its variability, which is central to reverberation mapping analysis.

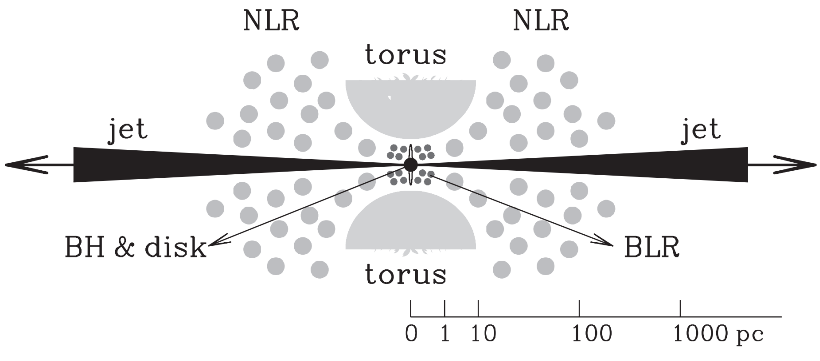

Figure 2.1: Different components of an AGN. Adopted from (Mo et al. 2010) Figure 14.3.

2.1.1 Structure and Spectral Features of an AGN

Figure 2.1 shows a schematic illustration of an AGN, consisting of a central supermassive black hole (SMBH), a surrounding accretion disk, a dusty torus and ionized gas regions known as the broad-line region (BLR) and narrow-line region (NLR). In some cases, relativistic jets are launched perpendicular to the plane of the accretion disk (Urry & Padovani 1995). The following subsections describe the physical components of AGN and the spectral features associated with them.

Supermassive Black Hole and Accretion Disk

The center of an AGN is defined by a supermassive black hole (SMBH), with typical masses between $10^6\,M_\odot$ and $10^9\,M_\odot$ (Peterson et al. 2004). It does not contribute to the AGN spectrum directly, but acts as the central engine driving observed spectral features of the AGN. It dominates the gravitational potential and, unlike inactive galaxies such as the Milky Way, it is surrounded by an accretion disk. Through viscous processes within the disk, such as turbulent friction and magneto-rotational instability, the angular momentum of the matter is transported outward, which leads to a spiraling inflow of matter toward the SMBH (Shakura & Sunyaev 1973). Several models have been proposed to describe the accretion process. The most widely used model is the geometrically thin and optically thick accretion disk, which consists of ionized gas in differential rotation around the SMBH (Shakura & Sunyaev 1973; Netzer 2013). The disk is composed primarily of ionized hydrogen and helium, with trace amounts of heavier elements (Netzer 2013). It extends from the innermost stable circular orbit (ISCO) near the event horizon out to distances of several light-days. The radial extent of the disk is relatively small compared to galactic scales and typically ranges from a few light-hours to a few light-days, corresponding to about 10^{-3} to 10^{-2} pc (Shakura & Sunyaev 1973; Netzer 2013).

During the accretion process a substantial fraction of the gravitational energy of the matter is transformed into thermal radiation, which accounts for the enormous luminosity observed in AGNs and heats the accretion disk to high temperatures that depend on the mass of the SMBH (Netzer 2013). For example, the maximum effective temperature for an accretion disk around a SMBH with $M = 10^8, M_\odot$ is on the order of several $\times 10^5$ K, leading to UV and optical emission (Shakura & Sunyaev 1973; Netzer 2013). By contrast, disks around stellar-mass black holes reach much higher temperatures (up to a few $\times 10^6$ K), and therefore emit mostly in X-rays (Shakura & Sunyaev 1973; Netzer 2013). Due to the radial temperature gradient, the emitted spectrum cannot be described as a single blackbody. Instead, it results from a superposition of many blackbody-like components at different temperatures, often referred to as a multicolour black-body (Netzer 2013). This produces a broad optical–UV continuum of ionizing photons, which interact with gas clouds near the nucleus and play a crucial role in shaping the spectral features of the BLR and NLR. These photons cause photoionization followed by recombination, which gives rise to the strong emission lines that are characteristic of AGN spectra (Netzer 2013).

Broad-Line and Narrow-Line Region

The ionized gas clouds near the nucleus can be divided into the broad-line region (BLR) and the narrow-line region (NLR). Both regions differ in density, distance from the SMBH, and the observed line widths (Urry & Padovani 1995). The BLR is located close to the nucleus, at distances ranging from a few light-days to a few light-years from the central SMBH (Goad et al. 2012)(see Figure 2.1). It consists of dense gas clouds with electron densities of $n_e \approx 10^{11}\,\mathrm{cm}^{-3}$, moving at velocities of several thousand $\mathrm{km\,s}^{-1}$ due to the strong gravitational influence of the SMBH. These velocities lead to significant Doppler broadening of permitted emission lines, with widths of (500–10,000) $\mathrm{km\,s}^{-1}$ (Peterson 1997). As described earlier, the BLR is photoionized by the continuum radiation emitted from the accretion disk. Consequently, the line emission from this region responds to changes in the continuum, leading to a strong correlation between the two and strong variability (Netzer 2013). This relationship is particularly relevant for reverberation mapping, which will be discussed later in Section 2.2.
Modelling the geometry of the BLR is challenging, because several emission lines have to be considered, whose intensities vary in response to changes in the continuum radiation (Netzer 2013). A common model assumes a spherical distribution of clouds connected to the accretion disk and located between the accretion disk and the dusty torus (Goad et al. 2012). Broad emission lines arise from permitted transitions such as Hα, Hβ, and Lyα (Netzer 2013).

The narrow-line region (NLR) extends out to several hundred parsecs from the central region (Peterson 1997). The gas in this region moves at much lower velocities, resulting in emission lines with widths typically of order (350–400) $\mathrm{km\,s}^{-1}$ (Peterson 1997). In contrast to the BLR, the NLR exhibits both permitted and forbidden transitions. Forbidden lines, such as [O III] λ5007, are prominent in the NLR because at its low densities ($n_e \sim 10^2$–$10^4\,\mathrm{cm}^{-3}$) collisional de-excitation is rare, allowing radiative decay from metastable levels (Peterson 1997). Due to its much larger extent compared to the BLR, the NLR responds only very slowly to variations in the ionizing continuum. Therefore, the flux of the narrow emission lines can be treated as constant over timescales of several years (Peterson 1993). Because permitted emission lines can also originate in the NLR, multi-component emission-line profiles can be observed in AGN spectra (Peterson 1997).

Dusty Torus

Surrounding the accretion disk and the broad-line region is the dusty torus, a geometrically thick, optically dense structure composed of gas and dust. It extends from the radius at which dust can survive the intense radiation from the accretion disk out to scales of a few parsecs (Netzer 2013). The torus likely has a clumpy distribution and plays a crucial role in the unified model of AGNs (Urry & Padovani 1995; Netzer 2013). The dust in the torus absorbs a significant fraction of the UV and optical radiation emitted by the accretion disk and re-emits it thermally in the infrared. As a result, AGNs typically exhibit strong infrared emission, with the peak wavelength depending on the dust temperature in the torus (Netzer 2013). Even when the central region is hidden from direct view by the torus, this reprocessed infrared emission remains observable. It therefore provides a characteristic signature of obscured AGN activity and enables indirect constraints on the otherwise hidden central engine (Netzer 2013).

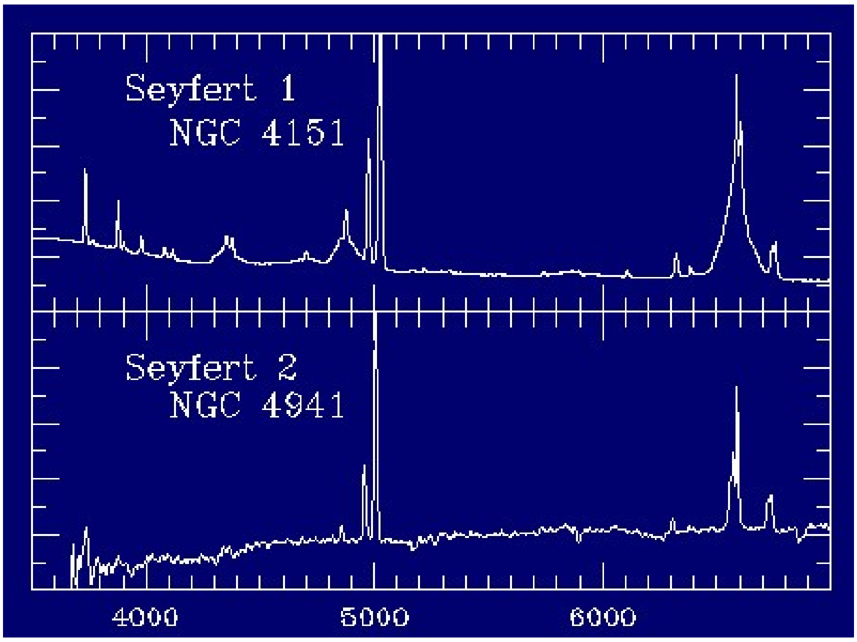

Figure 2.2: An example of Seyfert I and Seyfert II spectra illustrating their differences. Broad lines, such as the highlighted $H\alpha$ and $H\beta$, are only present in the Seyfert I spectrum, whereas forbidden [O III] lines are visible in both cases. Adapted from (Keel 2002).

2.1.2 Classification

AGNs get classified in subgroups based on their spectral features, which are strongly dependent to their intrinsic structure. The key parameters for this classification are luminosity, emission-line profiles and radio properties. Based on those parameters AGN get grouped into Seyfert galaxies, quasars and radio galaxies. They get further subdivided based on the appearance of broad and narrow emission lines. Some examples for these sub-classes are narrow-line Seyfert I galaxies (NLS1s), low-ionization nuclear emission-line regions (LINERs), and jet-dominated sources such as BL Lac objects or blazars (Antonucci 1993; Urry & Padovani 1995).

Seyfert Galaxies

Seyfert galaxies are named after Carl K. Seyfert, who in 1943 observed spiral galaxies characterized by exceptionally bright nuclei and strong emission lines in their optical spectra (Seyfert 1943). They are mainly classified into the sub-classes Seyfert I and Seyfert II based on the presence of broad emission lines. Figure 2.2 highlights the differences of the spectra of Type I and Type II Seyfert galaxies.
Seyfert I galaxies, such as NGC 4593, show both broad and narrow emission lines in their optical spectra. The broad lines, such as $H\alpha$ and $H\beta$, typically have full widths at half maximum (FWHM) of several thousand kilometers per second and from the fast-moving, high-density gas in the BLR (Peterson 1997). In contrast, narrow lines, including prominent forbidden transitions like [O III] λ5007 or [N II] λ6584, originate from the slow-moving, low-density gas in the NLR (Peterson 1997). The presence of both components in the spectrum allows for a clear classification as a Seyfert I galaxy, which is the case for NGC 4593. Further details on NGC 4593 are provided in Section 3.1. Between the two main Seyfert classes, several intermediate subclasses (1.2, 1.5, 1.8, 1.9) are defined based on the ratio of the broad towards the narrow components in the optical spectrum (Osterbrock 1977; Osterbrock 1981; Peterson 1997). Seyfert 1.8 and 1.9 galaxies show very weak broad components. In Seyfert 1.9 objects, the broad component is visible only in the Hα line, whereas in Seyfert 1.8 objects it is also detectable in Hβ. Furthermore, if the broad and narrow components in Hβ are of equal strength, the AGN is classified as a Seyfert 1.5 (Peterson 1997). If the narrow component is even weaker than the broad component, it is classified as a Seyfert 1.2 (Osterbrock 1977). The fact that the optical spectrum shows multi-component lines with both broad and narrow components, suggests that these emission lines originate in the BLR and the NLR in the respective ratio (Peterson 1997).

In comparison, Seyfert II galaxies completely lack these broad components in their optical spectra, likely due to orientation-dependent obscuration by the dusty torus. Following that the classification of a Seyfert galaxies strongly depends on the viewing angle of the observer, which is the key point for the Unified Model of AGN, which will deepened in section 2.1.3 (Peterson 1997).
Another notable subclass is the group of so-called narrow-line Seyfert I galaxies (NLS1s). They show most of the features of Seyfert 1 or 1.5 galaxies, except that the usually broad lines, such as the H I or He I lines, exhibit FWHM values that are only slightly larger than those of the narrow lines. They show a wide dispersion of spectral properties, with some objects have very strong Fe II emission, whereas others show almost none. This indicates that NLS1s do not form a homogeneous class (Osterbrock & Pogge 1985). NLSls are thought to have low-mass black holes accreting at high Eddington rates, suggesting they may represent a young evolutionary phase of AGN activity(Peterson 2011; Netzer 2013). Another possible explanation is an orientation effect. Another possible explanation is an orientation effect. When an NLS1 is observed at a very low inclination, the projected velocities are reduced, which leads to smaller observed Doppler broadening and therefore to narrow lines (Osterbrock & Pogge 1985).

Additional AGN Classes

In addition to Seyfert galaxies, there are several other classes of AGN. Quasars, which stands for quasi-stellar radio sources, are even more luminous than Seyfert galaxies and are typically found at higher redshifts. While the host galaxies of Seyfert galaxies are still observable, quasars completely outshine their host galaxies. Since quasars show similar emission characteristics to Seyfert galaxies, the modern distinction is based mainly on luminosity: quasars are classified as high-luminosity AGNs, while Seyfert galaxies represent the lower-luminosity end (Netzer 2013).
Radio galaxies form another important AGN class, distinguished by their strong radio emission and prominent jets, typically found in elliptical host galaxies. When their jets are aligned close to our line of sight, they are observed as blazars or BL Lac objects, which exhibit rapid variability and featureless optical spectra due to relativistic beaming (Netzer 2013).
Finally, LINERs are low-luminosity AGNs with spectra dominated by low-ionization emission lines. The physical origin of their ionization mechanism is still debated, and in some cases, they may not be powered by accretion at all (Netzer 2013).

While these classifications are based primarily on spectral characteristics, many of the observed differences between AGN types can be attributed to orientation effects. The Unified Model of AGN provides a framework that explains this apparent diversity through a common internal structure, viewed from different angles.

2.1.3 Unification Model

Figure 2.3 shows an illustration of the Unification Model, which was postulated by Robert Antonucci in 1993. He proposed that the visible differences in AGN spectra are not due to fundamentally different structures. Instead, they arise mainly from the viewing angle toward the AGN center and from obscuration by the dusty torus (Antonucci 1993).

The figure shows with what type the same AGN would get classified depending on the observers viewing angle. Like mentioned before, the dusty torus plays a key role here, as it surrounds the central region of the AGN, the accretion disk and the fast-moving BLR. If the observer's line of sight is blocked by the torus, only radio emission, the optical/UV continuum and narrow-line emission from the NLR outside the torus can be detected. In this case, the AGN is classified as a Seyfert 2 galaxy, as the broad emission lines originating from the BLR are obscured and the optical/UV continuum from the accretion disk is only partially visible. The observer essentially views the AGN from a flat angle, looking directly at the torus.If, on the other hand, the observer has a direct view into the central region of the AGN, not obscured by the torus, the fast moving gas clouds of the BLR as well as the optical/UV emission continuum from the accretion disk become visible. In this case, both broad and narrow emission lines are visible, meaning the AGN is classified as a Seyfert 1 galaxy. (Urry & Padovani 1995).

The same principle applies to other AGN classes. Quasars can be considered the high-luminosity counterparts of Seyfert galaxies, where orientation and torus obscuration likewise affect their observed properties. Blazars, on the other hand, are seen when the relativistic jet is aligned closely with the observer's line of sight, leading to strong Doppler boosting, which makes the radiation appear significantly brighter and shifted to higher frequencies than it intrinsically is (Urry & Padovani 1995).

Although the classical Unification Model treats AGN classification as fixed and purely geometry-driven, some AGNs have been observed to change their spectral type over time (Ricci & Trakhtenbrot 2023). These so-called "changing-look AGNs" demonstrate that a purely orientation-based interpretation, such as the Unification Model, cannot explain all observed phenomena. They suggest that intrinsic changes, such as variations in accretion rate or obscuring material, can also affect the classification (Ricci & Trakhtenbrot 2023).

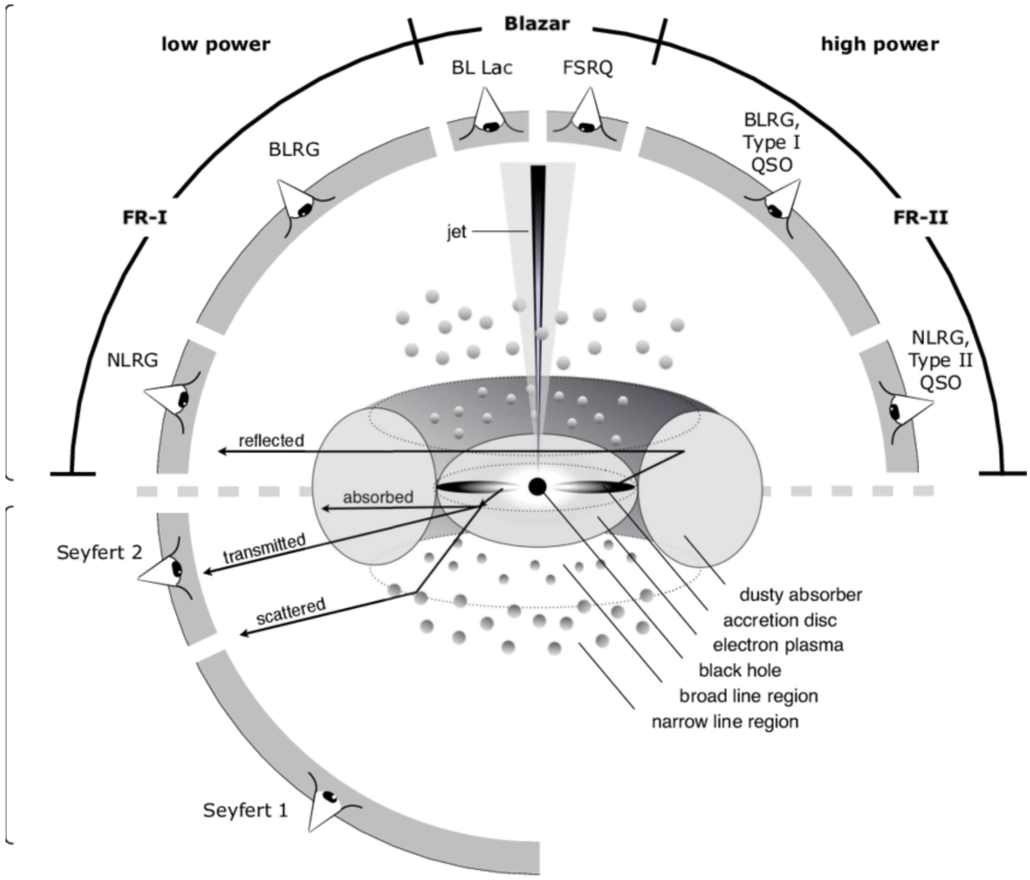

Figure 2.3: This graphic shows a schematic of the unification model of an AGN. The figure was adopted from (Beckmann & Shrader 2013).

2.1.4 Variability

The variability of active galactic nuclei (AGNs) is one of the key aspects that enables the study of their central regions, which generally cannot be probed with conventional spatially resolved observations. Variability is observed on timescales ranging from hours to several years and is generally stochastic, resulting in flux variations of both emission lines and continuum emission of up to a few tens of percent in the UV and optical bands (Ulrich et al. 1997; Ochmann et al. 2024). Although the origin of this variability is not yet fully understood, the most widely accepted models attribute it to inhomogeneities and instabilities within the accretion disk (Ulrich et al. 1997; Dexter & Agol 2010).

Depending on the underlying physical process, variations occur on different characteristic timescales. Processes such as thermal fluctuations or changes in the accretion flow happen on timescales of decades to centuries for typical SMBH masses and radii, and are therefore difficult to observe directly. In contrast, processes operating on shorter timescales are easier to study. Examples include gas motions and mechanical instabilities (e.g., sound waves) within the disk, which occur on timescales of weeks to months (Ricci & Trakhtenbrot 2023). The shortest timescale is the light-crossing timescale, $t_{\rm lc} = R/c$, which specifies how long light takes to traverse the emitting region (e.g., the broad-line region, BLR) (Ricci & Trakhtenbrot 2023). Here, c denotes the speed of light, and R denotes the characteristic size or radius of the variable emitting region. Following Ricci & Trakhtenbrot 2023, assuming a SMBH of mass $\approx 10^8\, M_\odot$, the light-crossing timescale can be written as

$$t_{\rm lc} = \frac{R}{c} \simeq 0.87 \left(\frac{R}{150\, r_g} \right) M_8 \, \text{days}, \tag{2.1}$$

where $r_g = GM/c^2$ is the gravitational radius of the black hole. Thus, the light-crossing timescale of the variable emitting region is of order days, and $t_{\rm lc}$ scales linearly with the size of the emitting region (Ricci & Trakhtenbrot 2023).
Because variations in the ionizing continuum occur on such short timescales, it is possible to measure delayed responses from other regions within the AGN that are correlated with the continuum, using long-term monitoring campaigns (Peterson 1997). In particular, the BLR responds to changes in the photoionizing continuum radiation of the central source with a time delay (lag) that is longer than the light-crossing timescale of the emitting region (Peterson 1997). This lag forms the basis of classical reverberation mapping, which will be further elaborated in the next section.

2.2 Reverberation Mapping

The main focus of this work is a classical reverberation mapping analysis of the broad lines of NGC 4593. Reverberation mapping probes the structure of the BLR around the SMBH by measuring the time delay (lag) between continuum variations and the correlated response of the broad lines. This lag can be used to constrain the BLR geometry and to estimate the SMBH mass (Cackett et al. 2018).

2.2.1 Principle of Reverberation Mapping

The fundamental assumption in reverberation mapping is that variations in the observed continuum flux are echoed by variations in the emission-line flux, with a measurable time delay (lag). When the continuum luminosity varies, the emission-line response follows with a measurable time lag (Cackett et al. 2021). The time lag τ corresponds to the average light-travel time between the photoionizing continuum source and the line-emitting regions. Assuming an idealized BLR consisting of spherically distributed clouds (Goad et al. 2012), then τ can be written as (Peterson

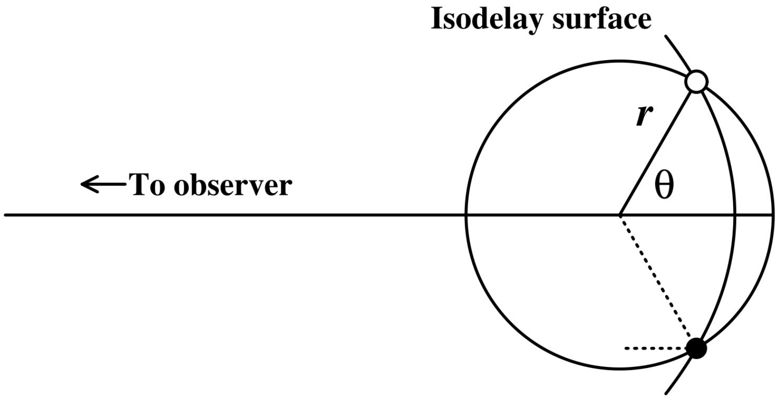

Figure 2.4: Spherical BLR model and an isodelay surface, adopted from (Peterson & Horne 2004).

1997)

$$\tau = (1 + \cos\theta) \cdot \frac{R_{\rm BLR}}{c}, \tag{2.2}$$

where $R_{\rm BLR}$ is the characteristic BLR radius, c is the speed of light, and θ is the angle between the line of sight and the position vector of the emitting gas with respect to the central source (see Figure 2.4) (Peterson 1997). The circle in Figure 2.4 represents the BLR modeled as spherical distribution of the clouds. For a fixed lag τ, the emitting regions that respond at that delay lie on a paraboloid aligned with the observer's line of sight, known as an isodelay surface. Therefore, emission observed at a given lag τ originates from the intersection of the BLR distribution with the corresponding isodelay surface (Peterson 1997). Thus, reverberation mapping can be used to "map" the BLR by inferring a characteristic BLR radius from the measured time lag (Peterson 1997). However, the observer receives emission from a range of delays (i.e., effectively from many isodelay surfaces), so the so-called transfer equation is required, which integrates over all delays (Peterson 1997):

$$L\left(t\right) = \int \Psi\left(\tau\right) C\left(t - \tau\right) d\tau. \tag{2.3}$$

Here, $\Psi(\tau)$ is the transfer function, which encodes the BLR geometry and kinematics, $C(t)$ is the continuum light curve, and $L(t)$ is the emission-line light curve (Peterson 1997). Although the BLR response is, in principle, fully described by the transfer function $\Psi(\tau)$, the lag is commonly estimated using cross-correlation techniques. In practice, recovering the full transfer function $\Psi\left(\tau\right)$ requires densely sampled, high signal-to-noise light curves spanning a duration much longer than the expected lag. Since real monitoring campaigns are often affected by observational gaps and noise, such reconstructions are rarely possible (Horne et al. 2004; Peterson

1993). For this reason, this project focuses on measuring the mean time lag between continuum and emission-line variations using the interpolated cross-correlation function (ICCF) method (Gaskell & Peterson 1987).

2.2.2 Lag Measurement

Using the notation of Peterson 1997, the cross-correlation function between the ionizing continuum and an emission line is defined as

$$F_{\mathrm{CCF}}(\tau) = \int_{-\infty}^{\infty} L(t)C(t-\tau)dt. \tag{2.4}$$

The auto-correlation function of the ionizing continuum is

$$F_{\mathrm{ACF}}(\tau) = \int_{-\infty}^{\infty} C(t)C(t-\tau)dt. \tag{2.5}$$

Together with the transfer equation (Equation 2.3), the cross-correlation function can be written as the convolution of the transfer function and the auto-correlation function of the ionizing continuum:

$$F_{\mathrm{CCF}}(\tau) = \int_{-\infty}^{\infty} \Psi(\tau')F_{\mathrm{ACF}}(\tau-\tau')d\tau'. \tag{2.6}$$

The lag is commonly defined as either the peak location (τ_{peak}) or the centroid (τ_{centroid}) of the CCF (Peterson 1997). While τ_{peak} is defined as the location of the CCF maximum, τ_{centroid} is calculated over all CCF points above a selected threshold, typically 80% of the peak value. Because the CCF is closely related to the transfer function, it is possible to infer a characteristic BLR size associated with the emission-line response (Peterson 1997), which can be expressed as

$$R_{\mathrm{BLR}} = c \cdot \tau_{\mathrm{centroid}}. \tag{2.7}$$

This follows from the light-travel timescale (Peterson et al. 2004). Since the centroid lag is generally considered a more robust estimator of the mean BLR light-travel time of the BLR (Peterson et al. 2004), it is used in this project.

The uncertainty of the measured lag is estimated using a Monte Carlo approach combining flux randomization (FR) and random subset selection (RSS) (Peterson et al. 1998; Peterson et al. 2004). In the FR step, each flux value is randomly perturbed according to its measurement uncertainty. In the RSS step, N data points are drawn randomly with replacement, while duplicate selections are discarded, resulting in a new light curve with $M \leq N$ points. For each realization, the ICCF analysis is repeated, yielding a distribution of centroid lags. The uncertainties are estimated from the distribution of centroid lags obtained from the simulations (Peterson et al. 2004). The 16th and 84th percentiles of this distribution are adopted as the bounds of the 1σ confidence interval (Peterson et al. 1998).

2.2.3 Black Hole Mass

The reverberation mapping method can be used not only to measure the characteristic size of the BLR, but also to estimate the mass of the central SMBH. Under the assumption that the gas dynamics in the BLR are dominated by the gravitational potential of the central SMBH, the black hole mass can be estimated using the virial theorem (Peterson et al. 2004).
The centroid time lag τ_{centroid} provides an estimate of the characteristic BLR radius via Equation 2.7. Together with the velocity dispersion ΔV of the BLR gas, the virial mass is given by

$$M_{\mathrm{vir}} = \frac{R_{\mathrm{BLR}}\,\Delta V^2}{G}. \tag{2.8}$$

The black hole mass is then given by

$$M_{\mathrm{BH}} = f \cdot M_{\mathrm{vir}}. \tag{2.9}$$

Here, G denotes the gravitational constant, and f is a scale factor that accounts for the unknown geometry, kinematics, and inclination of the BLR (Peterson et al. 2004).The velocity dispersion ΔV can be estimated from the widths of the broad emission lines (Peterson et al. 2004).
The scale factor f is calibrated by matching reverberation-based black hole masses to the empirical $M_{\mathrm{BH}} - \sigma_*$ relation observed in inactive galaxies, where σ_* denotes the stellar velocity dispersion of the galactic bulge (Onken et al. 2004). Different studies have reported values of f based on various AGN samples, for example, $f = 5.5$ (Onken et al. 2004), $f = 4.31$ (Grier et al. 2013), and $f = 3.6$ (Graham et al. 2011). The calibration of the scale factor also depends on the measurement method used for the line width of the broad emission lines (Peterson et al. 2004). Two commonly used measures are the line dispersion σ_{line} (see (Peterson et al. 2004)) and the FWHM. As this work focuses on the FWHM measures and the previously named scale factories where estimated with the line dispersion measure, a average scale factor of $f = 1.8$ gets adopted, following Probst et al. 2025. This value bases on the average scale factor $f = 3.6$ reported by Graham et al. 2011 and takes the relation FWHM/$\sigma_{\mathrm{line}} \approx 2$ Peterson et al. 2004 into account.

2.3 Bowen Fluorescence of OIλ8446

Previous studies of NGC 4593 report strong emission in the low-ionization lines OI λ8446 and the Ca II λ8498 λ8542 λ8662 triplet (Ochmann et al. 2025). In particular, O I λ8446 is of interest because it can be enhanced through a fluorescence mechanism referred to as Bowen fluorescence (Grandi 1980). The mechanism was first described by I.S. Bowen in 1934 to explain unexpected emission lines in nebular spectra. This mechanism describes a resonant line-pumping process in which photons emitted by one ion are absorbed by another ion of a different species via a permitted transition enabled by a near coincidence in wavelength between the pumping line and the absorbing transition. The resulting de-excitation leads to an enhancement of the emission lines (Bowen 1934).

One transition that can be enhanced by Bowen fluorescence is O I λ8446, which can be pumped by Lyβ photons (Netzer & Penston 1976). In this process, Lyβ photons at λ1025.72 Å are absorbed by neutral oxygen through the near-resonant transition $2p^4\,{}^3P_2 \rightarrow 3d\,{}^3D^0$ of O I at λ1025.77 Å. The excited $3d\,{}^3D^0$ level decays to $3p\,{}^3P$, which then decays to $3s\,{}^3S^{\circ}$, emitting the O I λ8446 emission line (see figure 2.5) (Grandi 1980). This provides an additional excitation channel for O I λ8446, in addition to recombination.

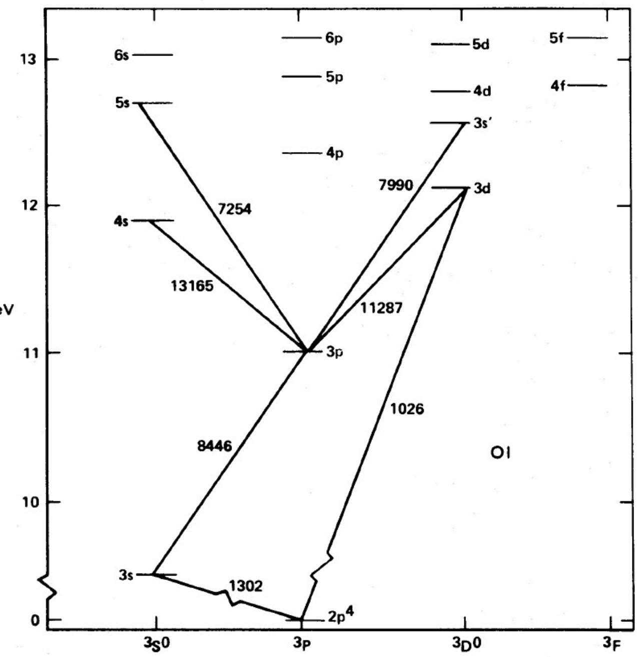

Figure 2.5: Energy level diagram displaying the process of Bowen fluorescence pumping of OI, adopted from (Grandi 1980).

3. Campaign and Data Preparation

The analysis of this campaign is based on the observation campaign of NGC4593 in 2016 by Cackett et al. 2018. This campaign took place between the 12th of July and the 6th of August with daily observations, which resulted in 26 successful out of 27 observations. It was performed with the Hubble Space Telescope (HST) using the Space Telescope Imaging Spectrograph (STIS) with the three different Gratings. The following section will cover an overview of the properties and specifications of NGC4593 and the campaign in 2016.

3.1 NGC4593

NGC 4593 is classified as a Seyfert 1 galaxy with a barred spiral morphology of type (R)SB(rs)b (Denney et al. 2006). It is located at RA = $12^{\mathrm{h}}39^{\mathrm{m}}39.44^{\mathrm{s}}$, Dec = $-05°20'39.03''$ (J2000) and has a redshift of $z = 0.0083 \pm 0.0005$, corresponding to a distance of $\sim 35.9\,\mathrm{Mpc}$ (Koss et al. 2022) assuming a ΛCDM cosmology. The galaxy exhibits a prominent large-scale bar and nuclear dust ring connected to dust lanes along the bar, as seen in Figure 3.1.

The AGN in NGC 4593 exhibits strong broad emission lines, including Balmer and Lyman lines as well as He, O, and Ca lines among others (Kollatschny & Dietrich 1997; Cackett et al. 2018; Ochmann et al. 2025). Several variability and reverberation-mapping campaigns have monitored different broad emission lines, including Kollatschny & Dietrich 1997; Denney et al. 2006. They reported FWHM values from the mean (AVG) and root-mean-square (RMS) spectra of their respective campaigns. The RMS spectrum is defined as the standard deviation of the flux at each wavelength across epochs:

$$F_{\mathrm{RMS}}(\lambda) = \sqrt{\frac{1}{N-1}\sum_{i=1}^{N}\left[F_i(\lambda) - \bar{F}(\lambda)\right]^2}, \tag{3.1}$$

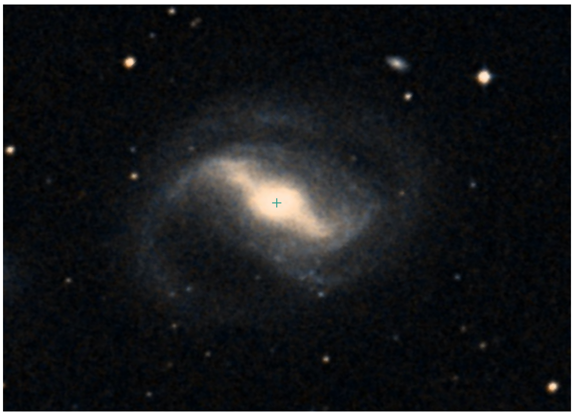

Figure 3.1: Screenshot of NGC 4593 visualized with Aladin Lite (*Aladin Lite* 2025) using DSS2 survey imagery (STScI 2025). The image is oriented with north up and east to the left. Right ascension increases to the left and declination increases upward.

with the mean spectrum at wavelength λ given by

$$\bar{F}(\lambda) = \frac{1}{N} \sum_{i=1}^{N} F_i(\lambda) \,. \tag{3.2}$$

Kollatschny & Dietrich 1997 measured $\mathrm{FWHM_{AVG/RMS}} = (3400 \pm 200)\,\mathrm{km\,s^{-1}}$ for Hα, while Denney et al. 2006 reported for Hβ $\mathrm{FWHM_{AVG}} = (5142 \pm 16)\,\mathrm{km\,s^{-1}}$ and $\mathrm{FWHM_{RMS}} = (4141 \pm 416)\,\mathrm{km\,s^{-1}}$. Based on these broad-line widths, they estimated the SMBH mass to be $M \approx 1.4 \times 10^7\,M_\odot$ (Kollatschny & Dietrich 1997) and $M = (9.8 \pm 2.1) \times 10^6\,M_\odot$ (Denney et al. 2006). Overall, these results suggest that the SMBH mass is of order $10^7\,M_\odot$.
Furthermore, NGC 4593 shows a rare double-peaked emission-line complex involving O I λ8446 and the Ca II λ8498, λ8542, λ8662 triplet (Ochmann et al. 2025). Ochmann et al. 2025 found that the Ca II triplet has an intensity ratio of 1:1:1 and line profiles that closely resemble those of O I λ8446, exhibiting a red-to-blue peak ratio of 4:3 and a FWHM of $\approx 3700\,\mathrm{km\,s^{-1}}$, suggesting that these lines originate in a similar high-density emission region. A fit of the asymmetric line profile of Ca II λ8662 with an elliptic accretion disk model, shows a eccentric of $e \approx 0.22$ and a low-inclination of $i \approx 11^\circ$ Ochmann et al. 2024.

3.2 The 2016 Hst Campaign

The campaign of Cackett et al. 2018 was designed to study wavelength-dependent continuum lags. It took place between the 12th of July and the 6th of August with daily observations, which resulted in 26 successful out of 27 observations. Observations were carried out with the Hubble Space Telescope (HST) using the Space Telescope Imaging Spectrograph (STIS) and three different gratings. The low-resolution STIS gratings provided continuous spectral coverage over a broad wavelength range. In each observation, spectra were obtained using the G140L, G430L, and G750L. All spectra were acquired with the $52'' \times 0.2''$ slit.

The characteristics of the STIS gratings used in this work are summarized in Table 3.1. After standard pipeline processing, charge-transfer inefficiency (CTI) corrections were applied using an algorithm based on (Anderson & Bedin 2010). Remaining hot pixels were removed manually by interpolating the flux from neighboring pixels.

Table 3.1: Overview of STIS grating characteristics (Institute 2025).

Grating	**Range [Å]**	**Exp. Time [s]**	**Res. Power**	**Dispersion [Å/pixel]**
G140L	1119–1715	1234	~ 1000	0.6
G430L	2888–5697	298	$\sim 500 - 1000$	2.73
G750L	5245–10233	288	$\sim 500 - 1000$	4.92

3.3 Intercalibration and Determination of AVG and RMS Spectra

Reverberation mapping requires multiple epochs to capture variability. For the 2016 campaign of NGC 4593, we retrieved 27 spectra from the *Hubble Advanced Spectral Products (HASP)* 2025 archive using the HASP search form in *Mikulski Archive for Space Telescopes (MAST)* 2025 . 26 of these spectra are usable for further analysis. The top panel of Figure 3.2 shows all spectra in the spectral range from 4000Å to 9000Å.

For the subsequent analysis, the average spectrum (AVG) is obtained by averaging over all epochs, improving the signal-to-noise ratio (S/N). Furthermore it is essential for the reverberation mapping analysis to identify variability between the epochs, which can be assessed with the root-mean-spuare (RMS) spectrum, defined as the standard deviation of the flux at each wavelength across epochs (see. Equation 3.1). Constant features, such as narrow emission lines, vanish in the RMS spectrum, leaving only variable components such as broad emission lines. The top panel of Figure 3.2 shows the AVG and RMS spectra from the original retrieved data. Residual variability is still noticeable in nominally non-varying lines, particularly in the forbidden line [O III] λ5007. This indicates small wavelength misalignment between epochs.

Therefore, an intercalibration anchored to the narrow [O III] $\lambda5007$ line was performed. This was achieved by shifting the wavelengths of the individual spectra and scaling the line flux to a constant value. As a narrow line, the flux of [O III] $\lambda5007$ can be assumed to remain constant over the timescale of the campaign. Based on this assumption, the flux of each spectrum was scaled to $(106 \pm 5) \times 10^{-15}\,\mathrm{erg\,s^{-1}\,cm^{-2}}$ and the wavelength was shifted by a maximum of 1Å.
Figures 3.2 shows a comparison of the original and the intercalibrated epochs and the corresponding AVG and RMS spectra. The disappearance of narrow features in the calibrated RMS spectrum, especially the [O III] $\lambda5007$ line, confirms that the apparent variability in the RMS of the original epochs was induced by the wavelength shifts between them, rather than intrinsic line variability. However the intercalibration was only applied to the optical part of the spectra due to its limited reliability. In the following analysis, the intercalibrated AVG and RMS spectra are used for the optical range obtained with the G430L and G750L gratings, while the AVG and RMS spectra from the original epochs are used for the UV emission-line analysis, as these were acquired with the G140L grating.

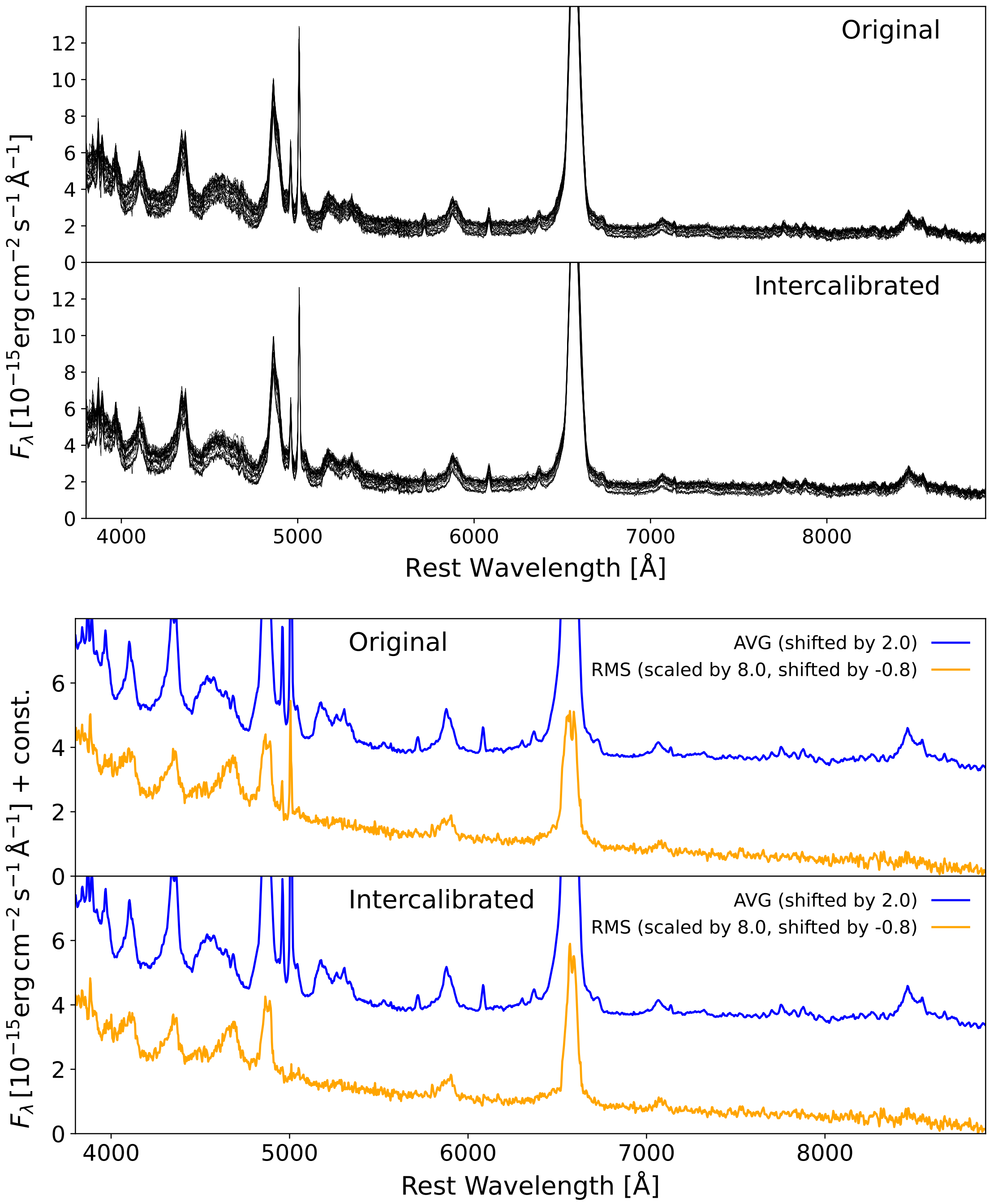

Figure 3.2: Comparison of the spectral range between 4000Å and 9000Å from the 2016 HST campaign of NGC 4593, showing the effects of [O III] λ5007 intercalibration on both the individual spectra (top) and the derived average and rms spectra (bottom).

4. Reverberation Mapping Analysis of NGC4593

4.1 Line Identification

The first step of the reverberation mapping analysis is the identification of emission and absorption lines within the AVG spectrum. Figures 4.1 and 4.2 show the optical to near-infrared range between 3900Å and 9000Å and the UV range between 1100Å and 1700Å, respectively. Looking at Figure 4.1, it is possible to identify prominent broad emission lines in the AVG spectrum are the Balmer-Lines up to Hϵ, with Hα being the strongest followed by Hβ and Hγ, and several He-emission lines such as He Iλ4471, He II λ4685, the He I λ5015, He I λ5875, He I λ7065. Another significant broad emission line complex appears in the NIR part of the spectrum, including the O I λ8446 emission line and the Ca II λ8498 λ8542 λ8662 triplet. All of those lines show significant variation in the RMS, especially the Balmer-lines and the He II λ4685 and He I λ5875 with very good distinguishable profiles. The He Iλ4471, the He I λ5015, the He I λ7065, the O I λ8446 emission line and the Ca II λ8498 λ8542 λ8662 triplet show smaller but still noticeable variation. The He Iλ4471 and He I λ5875 lines are blended with a Fe II emission line group in the AVG, which is vanishing in the RMS, as it shows no variation. The same aplies to the Fe II emission line group around 5200 Å.

Apart from the broad emission lines, the AVG spectrum shows strong forbidden [O III] narrow emission lines. [O III] λ5007 and [O III] λ4958 are strong enough to be distinguishable, while the [O III] λ4363 blends with Hγ. As narrow lines they and several more weaker narrow lines, show no variability in the RMS spectrum over the period of the campaign.

The campaign also included an UV spectrum between 1000 Åand 1700 Å, which is shown in Figure 4.2. The most prominent broad lines in the UV spectrum are the Lyα line, which is blended with the N V $\lambda\lambda$1238, 1242 duplet, the Si IV$\lambda\lambda$1393, 1402 duplet, which is blended with a partly forbidden O IV] line, and the C IV$\lambda\lambda$1548, 1550

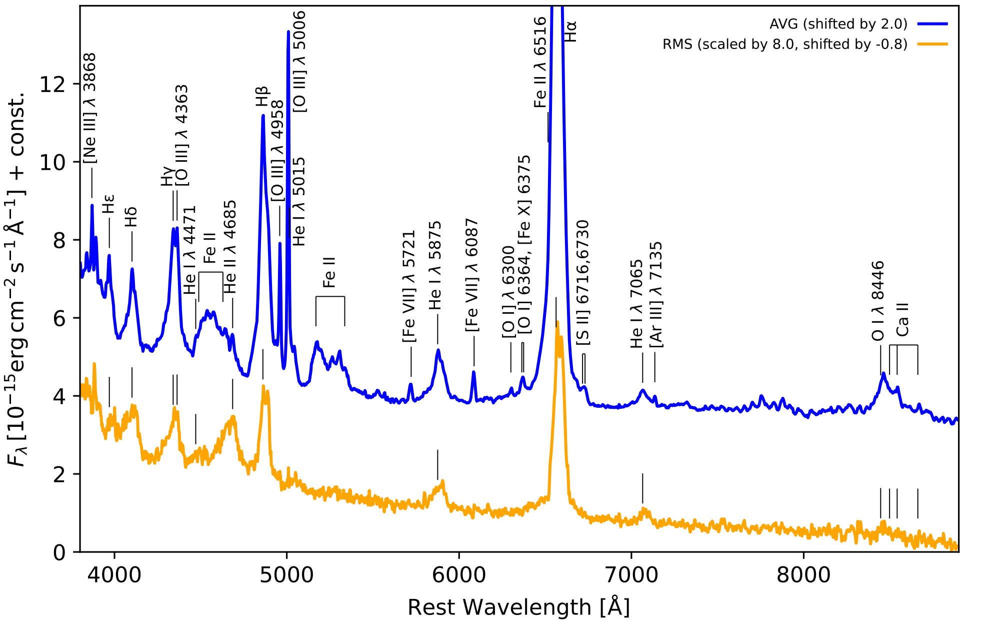

Figure 4.1: Optical-to-NIR AVG and RMS spectrum with identified emission lines.

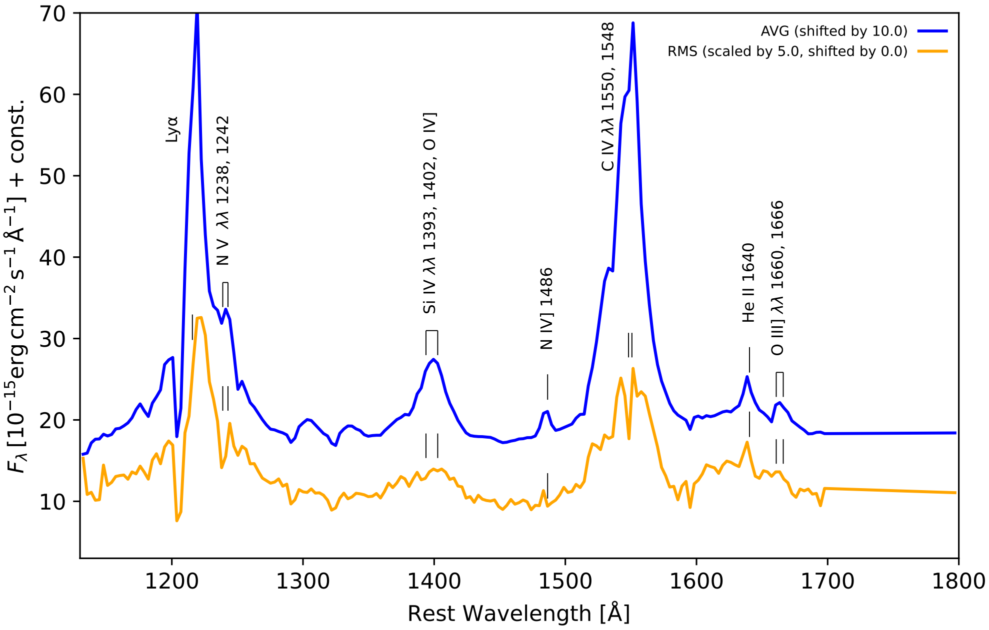

Figure 4.2: UV spectrum AVG and RMS spectrum with identified emission lines

duplet. They all show strong variation in the RMS spectrum. Apart of the strong lines, a weaker variable Helium II line can be identified at 1640 Å.
The Bowen fluorescence of O I $\lambda 8446$, which is investigated in this analysis, is typical driven by the emission of the Lyβ line (Grandi 1980), which lies outside the spectral range of the HST Campaign. However, as can be seen in figure 4.2, Lyα still lies in the spectral range of the campaign, as the bluest broad line of the taken spectra. As Lyα and Lyβ are assumed to originate in the same physical region, Ly$_\alpha$ can be used to examine the correlation of O I $\lambda 8446$ and Lyα for Bowen fluorescence.

4.2 Emission Line and Continua Measurement

After identifying the emission lines, the next step of the analysis is to measure the fluxes of those lines. This is done with the help of a python-based tool called GECHO created by M. Probst. It enables to import full campaigns, determine the AVG and RMS spectra, extracting lightcurves and do further measurements, naming here line-width measurements and lags measurement using the ICCF methode (Gaskell & Peterson 1987; Peterson et al. 2004), which will be further discussed in Section 4.4 and 4.5.
With help of GECHO the flux density gets integrated over the extent of each emission line for every observed spectrum of the campaign. Here it is important to define the integration limits so that all of the emission line flux is measured in this way. To ensure this, a parallel view of the AVG- and RMS-spectrum was used to define those integration limits, and to ensured, that no component of any other line is contributing to the line flux of the measured line. Additionally, the integration boundaries get selected, making sure they span a similar area in velocity space for every emission line. To accounting the surrounding continuum a linear underlying continuum gets interpolated and subtracted first. For this interpolation, sections on the blue and red side of the emission line with no line contribution gets selected. The chosen integration limits and pseudo-continua are listed in Table 4.1.
To measure the delay between the ionizing continuum and the emission lines it is necessary to extract lightcurves of selected continua in the AVG spectrum. Continua lightcurves are getting extracted by measuring the mean flux density of a sufficiently large region without line emission or absorption. The chosen integration limits for the continua can be found in Table 4.2.

Table 4.1: Integration Limits and Pseudo-Continua of the measured emission lines

Line	**Integration Limits** [Å]	**Pseudo-Continua** [Å]
Lyα	$1207 - 1238$	$1151 - 1161, 1461 - 1469$
NV $\lambda\lambda$1238, 1242	$1207 - 1238$	$1151 - 1161, 1461 - 1468$
SiIV $\lambda\lambda$1393, 1402	$1358 - 1423$	$1151 - 1161, 1461 - 1469$
CIV $\lambda\lambda$1548, 1550	$1511 - 1578$	$1461 - 1469, 1680 - 1685$
HeII λ1640	$1599 - 1645$	$1461 - 1468, 1680 - 1685$
Hα	$6453 - 6695$	$6107 - 6129, 6861 - 6900$
Hβ	$4779 - 4944$	$4762 - 4774, 5085 - 5112$
Hγ	$4230 - 4427$	$4197 - 4220, 4435 - 4450$
HeI λ5875	$5742 - 6039$	$5645 - 5653, 6044 - 6057$
HeII λ4685	$4545 - 4758$	$4435 - 4450, 4762 - 4774$
OI λ8446	$8380 - 8498$	$8005 - 8031, 8850 - 8955$
OIII λ5007	$4982 - 5033$	$4762 - 4774, 5085 - 5112$

Table 4.2: Integration Limits of the measured continua

Line	**Integration Limits** [Å]
Cont. 1150	$1151 - 1161$
Cont. 4010	$4026 - 4033$
Cont. 4440	$4435 - 4450$
Cont. 5100	$5085 - 5112$
Cont. 6110	$6107 - 6129$
Cont. 6880	$6861 - 6900$
Cont. 8015	$8005 - 8031$
Cont. 8900	$8864 - 8955$

4.2.1 Variability Statistics

To quantify the variability of the emission lines and continua variability statistics the definition by Rodriguez-Pascual et al. 1997 are adopted. They name the maximum-to-minimum flux ratio R_{max} and the fractional variability F_{var} as two common measures of variability. R_{max} is defined as the ratio of the the extreme of the integrated fluxes, F_{min} and F_{max}, and F_{var} as:

$$F_{\mathrm{var}} = \frac{\sqrt{\sigma_F^2 - \Delta^2}}{\langle F \rangle} \tag{4.1}$$

Here, σ_F^2 denotes the standard deviation, $\langle F \rangle$ the mean flux and Δ^2 the mean square value of the flux uncertainties, which is defined by:

$$\Delta^2 = \frac{1}{N} \sum_{i=1}^{N} \Delta_i^2 \tag{4.2}$$

The results for all parameters can be found in the Tables 4.3.
First, considering R_{max} and F_{var} of the continuum lightcurves, all measured continua show similar variability, except for the UV continuum around 1150 Å, which shows significantly higher variability with $R_{\mathrm{max}} = 2.58$ and $F_{\mathrm{var}} = 0.28$ than the optical and NIR continua. These continua show a fairly uniform variation between $R_{\mathrm{max}} \simeq 1.33 - 1.59$ and $F_{\mathrm{var}} \simeq 0.08 - 0.14$.
The lightcurves of the Balmer emission lines exhibit lower variability, which increases towards the higher-order Balmer lines, with values between $R_{\mathrm{max}} \simeq 1.15 - 1.52$ and $F_{\mathrm{var}} \simeq 0.03 - 0.1$. The helium lightcurves show a similar variability to Hδ with values between $R_{\mathrm{max}} \simeq 1.48 - 1.62$ and $F_{\mathrm{var}} \simeq 0.09 - 0.11$ and the OI λ8446 a similar variability to the lower-order balmer lines with $R_{\mathrm{max}} \simeq 1.22$ and $F_{\mathrm{var}} \simeq 0.04$.
The variability of the emission line lightcurves in the UV region is on a similar level as that of the helium light curves in the optical region, with $R_{\mathrm{max}} \simeq 1.42 - 1.62$ and $F_{\mathrm{var}} \simeq 0.14$, with the exception of the HeII, λ1640 lightcurve, which shows significant higher variability with $R_{\mathrm{max}} \simeq 3.12$ and $F_{\mathrm{var}} \simeq 0.31$.

Table 4.3: Variability statistics of the measured continua and emission lines with minimum flux(2) and maximum flux density or integrated flux (3), peak-to-peak ratio (4), mean (5), standard deviation (6) and fractional variation (7).

Continuum/Line (1)	F_{min} (2)	F_{max} (3)	R_{max} (4)	$\langle F \rangle$ (5)	σ_F (6)	F_{var} (7)
Cont. 1150	0.52	1.35	2.58	0.86	0.25	0.28
Cont. 4010	2.68	4.21	1.57	3.49	0.47	0.14
Cont. 4440	2.42	3.73	1.54	3.14	0.39	0.12
Cont. 5600	1.36	2.15	1.59	1.82	0.25	0.14
Cont. 6110	1.49	2.27	1.53	1.9	0.23	0.12
Cont. 6880	1.33	2.01	1.5	1.72	0.2	0.11
Cont. 8015	1.18	1.69	1.43	1.48	0.15	0.1
Cont. 8900	1.14	1.52	1.33	1.38	0.11	0.08
Hα	130.83	149.85	1.15	141.35	4.83	0.03
Hβ	38.29	45.4	1.19	42.32	1.94	0.05
Hγ	18.82	24.38	1.3	21.91	1.29	0.06
Hδ	7.17	10.92	1.52	9.13	0.94	0.1
HeII λ4685	11.93	17.7	1.48	14.82	1.6	0.11
HeI λ5875	8.53	13.82	1.62	11.58	1.01	0.09
OI λ8446	7.47	9.13	1.22	8.32	0.37	0.04
Lyα	66.87	94.88	1.42	82.21	8.03	0.1
SiIV $\lambda\lambda$1393, 1402	21.93	35.5	1.62	27.92	3.88	0.14
CIV $\lambda\lambda$1548, 1550	115.31	165.57	1.44	138.77	12.12	0.09
HeII λ1640	6.83	21.29	3.12	13.29	4.13	0.31

4.2.2 Uncertainties Estimation

The uncertainties of the continuum and emission-line lightcurves are estimated from two components. The first component originates from the noise in the flux densities over the pixels within the integration bounds, N_{pixel}. For the continuum lightcurves, the noise uncertainty is estimated as

$$\sigma_{\mathrm{noise}}^{\mathrm{cont}} = \frac{\sigma_F}{\sqrt{N_{\mathrm{pixel}}^{\mathrm{cont}}}}, \tag{4.3}$$

where σ_F denotes the standard deviation of the flux density within the selected continuum window. Since the emission-line lightcurves are extracted by integrating the continuum-subtracted flux density, the corresponding noise uncertainty is estimated using the noise measured from the used pseudo-continua, $\sigma_{\mathrm{noise}}^{\mathrm{p.cont.}}$:

$$\sigma_{\mathrm{noise}}^{\mathrm{lines}} = \frac{\sigma_{\mathrm{noise}}^{\mathrm{p.cont.}} \cdot \Delta\lambda}{\sqrt{N_{\mathrm{pixel}}^{\mathrm{line}}}}. \tag{4.4}$$

Here, $\Delta\lambda$ denotes the integration window used for the emission line, and $N_{\mathrm{pixel}}^{\mathrm{line}}$ denotes the number of pixels within this window.

The second component originates from the intercalibration of the epochs of the campaign. The flux of each epoch is scaled based on the narrow emission line [O III] $\lambda 5007$, which is assumed to be constant over the campaign. To account for the systematic uncertainty introduced by the intercalibration, the fractional variability of [O III] $\lambda 5007$ is multiplied by the integrated flux values f_i and used as a proxy for the intercalibration uncertainty:

$$\sigma_i^{\mathrm{cal.}} = F_{\mathrm{var}}^{[\mathrm{O\,III}]\,\lambda 5007} \cdot f_i. \tag{4.5}$$

This yields the total light-curve uncertainty:

$$\sigma_i = \sqrt{(\sigma_i^{\mathrm{cal.}})^2 + (\sigma_{\mathrm{noise}})^2}, \tag{4.6}$$

where σ_{noise} corresponds to $\sigma_{\mathrm{noise}}^{\mathrm{cont}}$ for continuum light curves and to $\sigma_{\mathrm{noise}}^{\mathrm{lines}}$ for emission-line light curves.

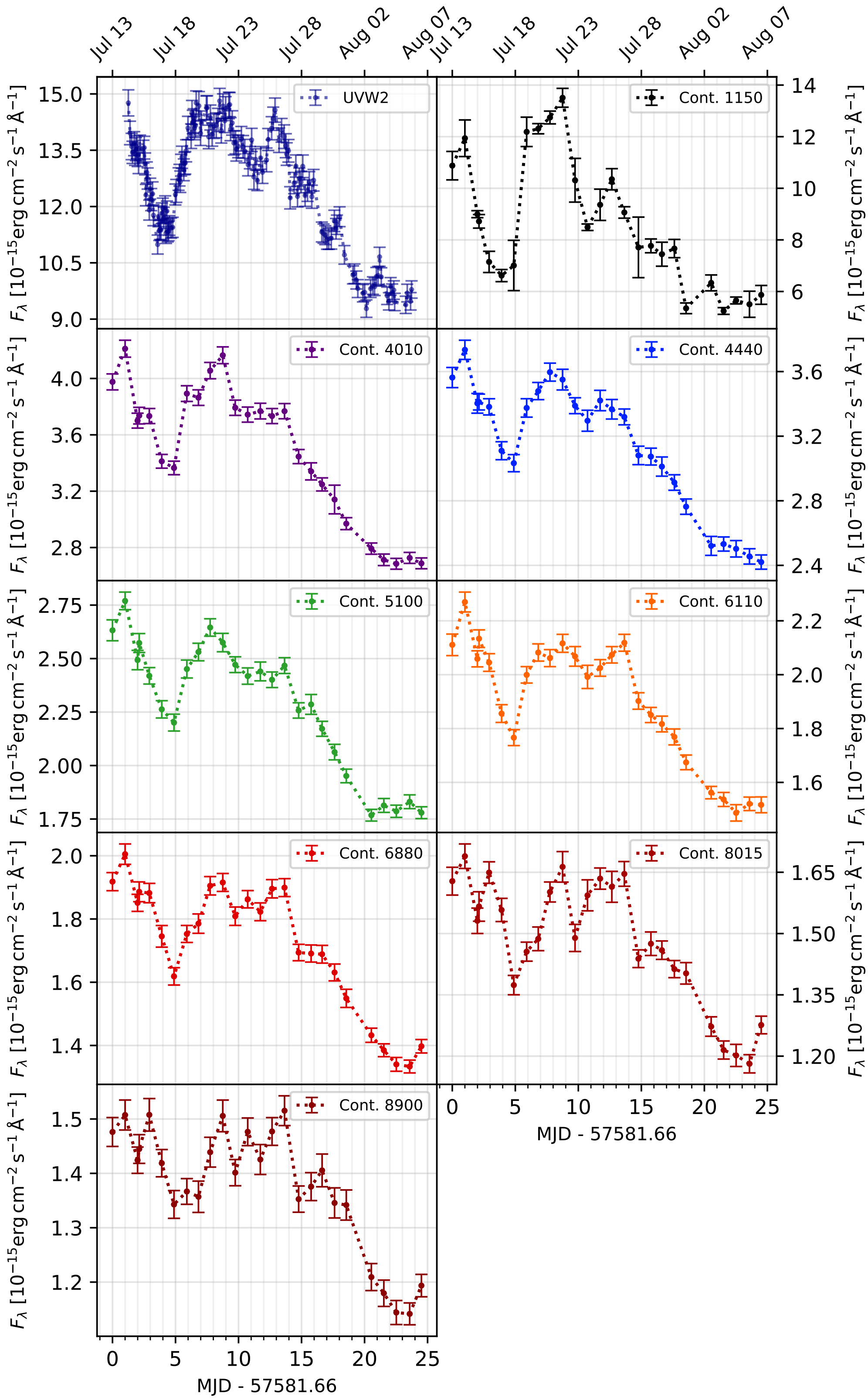

Figure 4.3: Comparison of the continua lightcurves. The first panel shows the UVW2 continuum lightcurve obtained from McHardy et al. 2018, while the other panels show the measured continua defined in Table 4.2

4.3 Lightcurves

The extracted lightcurves of the continua and emission lines are shown in Figures 4.3, 4.4, and 4.5. In addition to the measured lightcurves of the HST campaign, the UVOT UVW2 lightcurve taken with *Swift* by McHardy et al. 2018, which was also used in Cackett et al. 2018, is included in this analysis, as it has a higher sampling rate than the light curves of the HST campaign. The spectra were taken during nearly every orbit for 6.4 d between July 13 and July 18, 2016 (McHardy et al. 2018). The central wavelength of the UVW2 lightcurve is located at about 1930 Å (McHardy et al. 2018).

When compared, all measured continuum lightcurves show a roughly similar shape (see Figure 4.3). The lightcurves start at a high flux level, followed by a significant decrease of about 50–80% relative to the maximum-to-minimum range of each curve approximately between the 1st and 6th day, with the minimum at around the 4th day. A central region follows, with again high flux with variation depending on the wavelength range of the continua. For the UV continua, this plateau ranges from the 6th to the 9th day and is followed by another smaller decrease in flux between the 9th and 13th day, before it increases again with peak at around the 13th day. Subsequently, the flux decreases, with small interim variation, towards a minimum at the end of the campaign. The continua between 4010 Å and 6110 Å also show a plateau-like shape between the 6th and 14th day, except for a small increase in flux between the 7th and 10th day, before decreasing again. The red and NIR continua show a roughly constant plateau between the 8th and 14th day, before decreasing in the same way as the other light curves, with another small, more pronounced flux plateau between the 15th and 17th day.

One goal of this reverberation mapping analysis is to estimate the physical distance between the SMBH and the region from which the emission lines originate. Assuming that the continuum radiation originates from the accretion disk, it is common to use the bluest available continuum as reference for the time lag estimation, which is expected to originate closest to the SMBH (Ochmann et al. 2026). In this case, this would be the continuum around 1150 Å. Nevertheless, the UVW2 continuum was selected as the main reference lightcurve for the subsequent analysis due to its higher sampling rate. To accommodate this, the delay between the UV continuum lightcurve around 1150 Å and the UVW2 lightcurve has to be taken into account.

Figures 4.4 and 4.5 show the lightcurves of the measured broad emission lines in the optical-to-NIR range and in the UV range. Overall, the light curves show a similar shape to the UVW2 lightcurve: a high or increasing flux in the first few

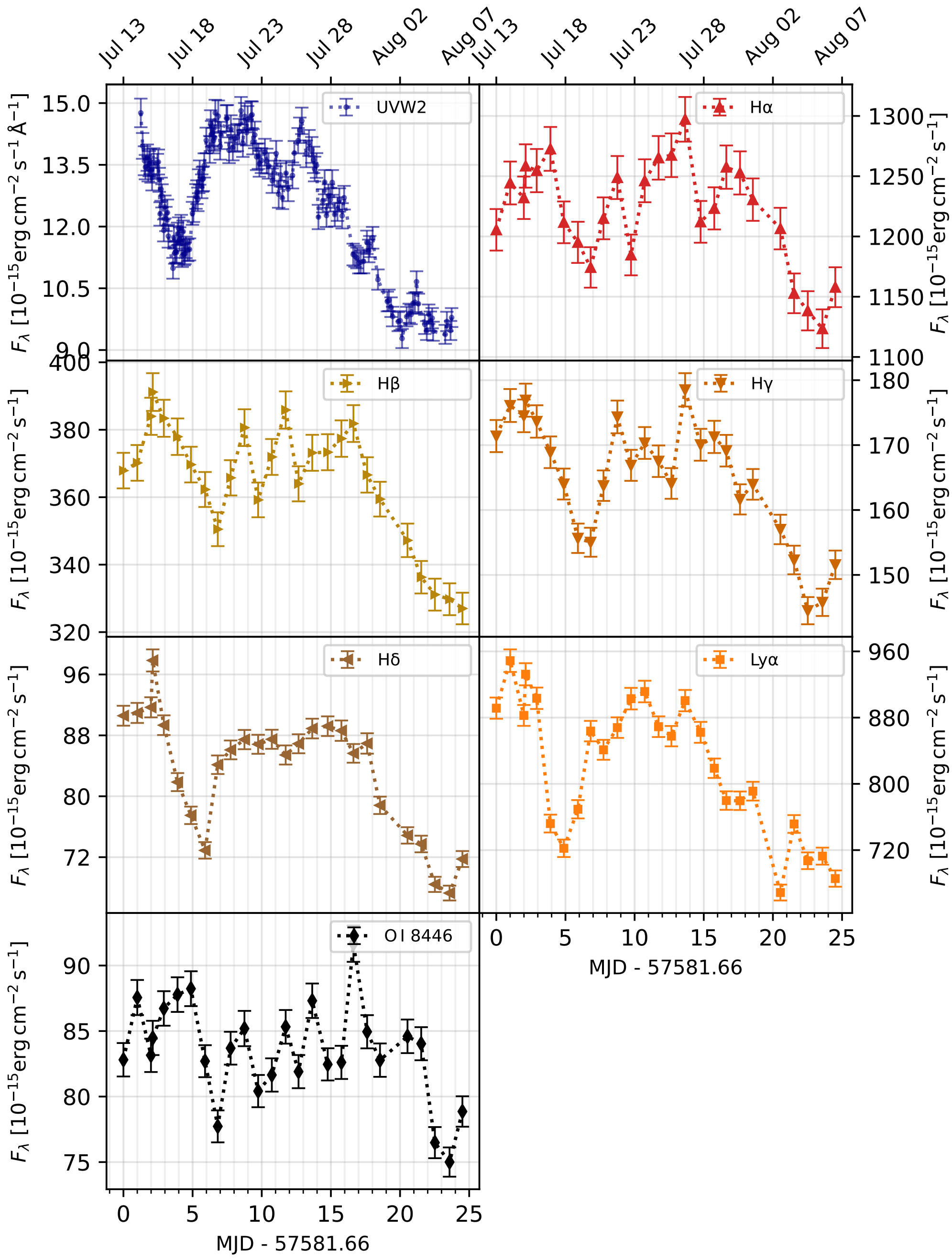

Figure 4.4: Comparison of the emission-line lightcurves to the UVW2 reference lightcurve in the first panel. The UVW2 lightcurve was obtained from McHardy et al. 2018

days, a pronounced minimum, a plateau-like central part that is fluctuating in some cases, and a decrease towards the end of the campaign. The main exceptions are the OI $\lambda 8446$ and HeII $\lambda 1640$ lightcurves, which are much more scattered than the others. Nevertheless, it is possible to notice a pronounced minimum similar to that in the UVW2 light curve in these curves. By comparing these features, a shift of

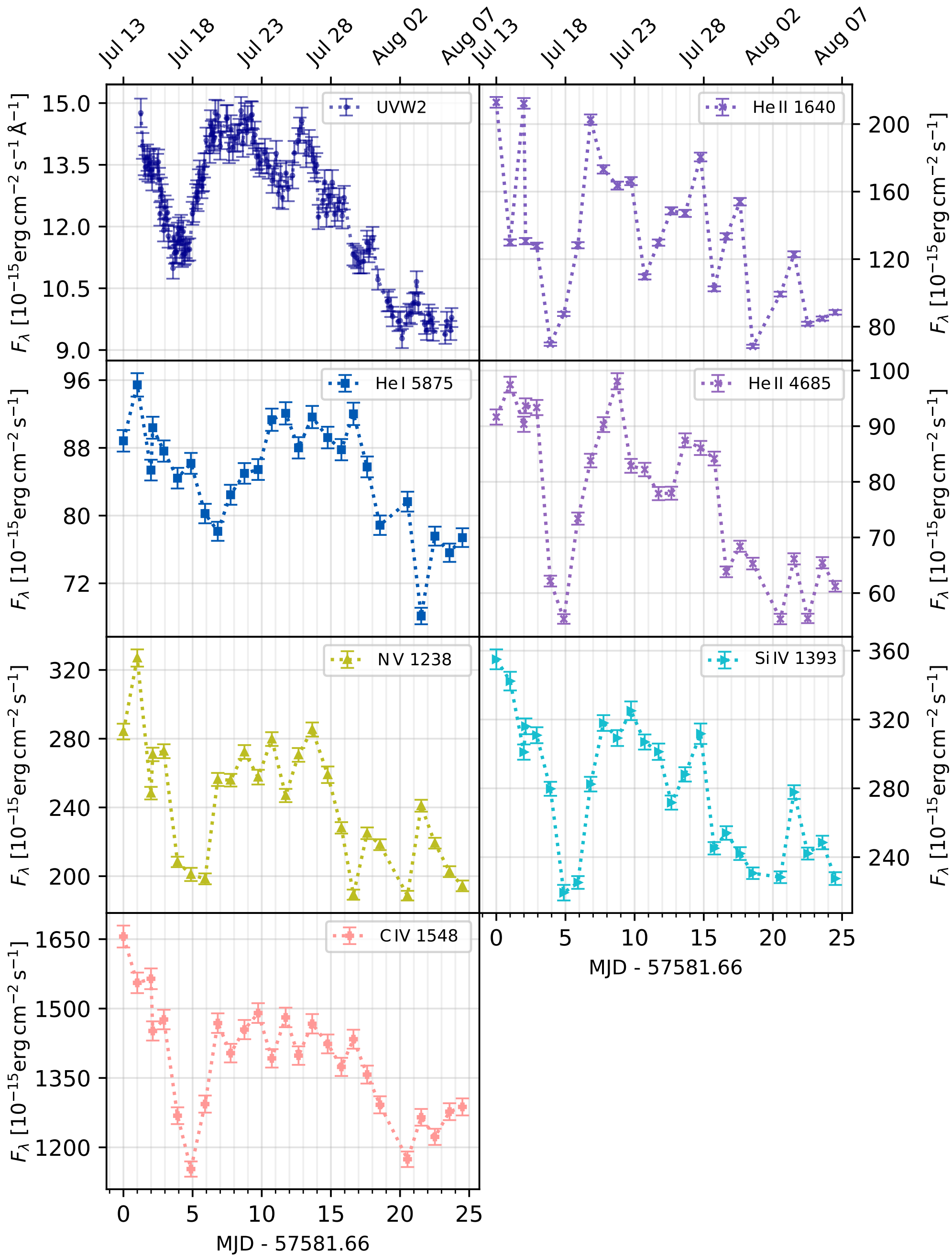

Figure 4.5: Comparison of the emission-line lightcurves to the UVW2 reference lightcurve in the first panel. The UVW2 lightcurve was obtained from McHardy et al. 2018

a few days between the light curves is already apparent. The flux minima of the Balmer lines, OI λ8446, and HeI λ5875 occur between days 6 and 7, whereas the minima of the HeII light curves and the UV emission lines Lyα, SiIV $\lambda\lambda$1393, 1402, and CIV $\lambda\lambda$1548, 1550 occur between days 4 and 5. This provides a first estimate of a time lag of about 2–3 days for the first group of emission lines and about 0–1 days for the second group. A more detailed investigation of the time lags is presented in Section 4.5.

4.4 Line Profiles

The next step of the analysis is the extraction of line profiles of the broad emission lines from both, the AVG and RMS spectrum. By investigation their shape and line width it allows conclusions about the kinematics of the region their originated from. Following the same procedure as for the lightcurve extraction, an underlying linear continuum is interpolated using a chosen blue and red pseudo-continuum for each line in both the AVG and RMS spectra. The selected boundaries of the pseudo-continua are listed in Table 4.4. By subtracting this interpolated continuum, a new zero-flux baseline for each line profile gets defined, which allows a better comparison between the line profiles.

Table 4.4: Boundaries of the blue and red pseudo-continua used for the interpolation of underlying continua for line profile extraction.

Line	**Pseudo-Continua AVG** [Å]	**Pseudo-Continua RMS** [Å]
Hα	$6194-6216, 6861-6900$	$6279-6301, 6742-6781$
Hβ	$4762-4774, 5085-5112$	$4762-4774, 4967-4984$
Hγ	$4197-4220, 4435-4450$	$4197-4220, 4417-4429$
Hδ	$4026-4033, 4197-4221$	$4006-4016, 4197-4211$
O I λ8446	$7999-8025, 8775-8798$	$8222-8238, 8748-8767$
He I λ5875	$5679-5697, 6044-6057$	$5736-5753, 6027-6045$
He II λ1640	$1461-1468, 1679-1685$	$1461-1468, 1679-1685$
He II λ4685	$4198-4225, 4762-4774$	$4543-4554, 4766-4778$
Lyα	$1151-1161, 1270-1285$	$1151-1161, 1340-1355$
N V $\lambda\lambda$1283, 1242	$1151-1161, 1270-1285$	$1151-1161, 1340-1355$
Si IV $\lambda\lambda$1393, 1402	$1350-1360, 1430-1440$	$1340-1355, 1430-1440$
C IV $\lambda\lambda$1548, 1550	$1461-1468, 1679-1685$	$1461-1468, 1679-1685$

Subsequently, the line profile is converted to velocity space using

$$v_i = c \cdot \frac{\lambda_i^2 - \lambda_{\text{central}}^2}{\lambda_i^2 + \lambda_{\text{central}}^2}. \tag{4.7}$$

Here, λ_i denotes the wavelength values, λ_{central} the central wavelength of the emission line in rest-frame and c the speed of light. Finally, the flux is getting normalized to the maximum of each line profile. Figure 4.6 shows an overview of the extracted and normalized line profiles.

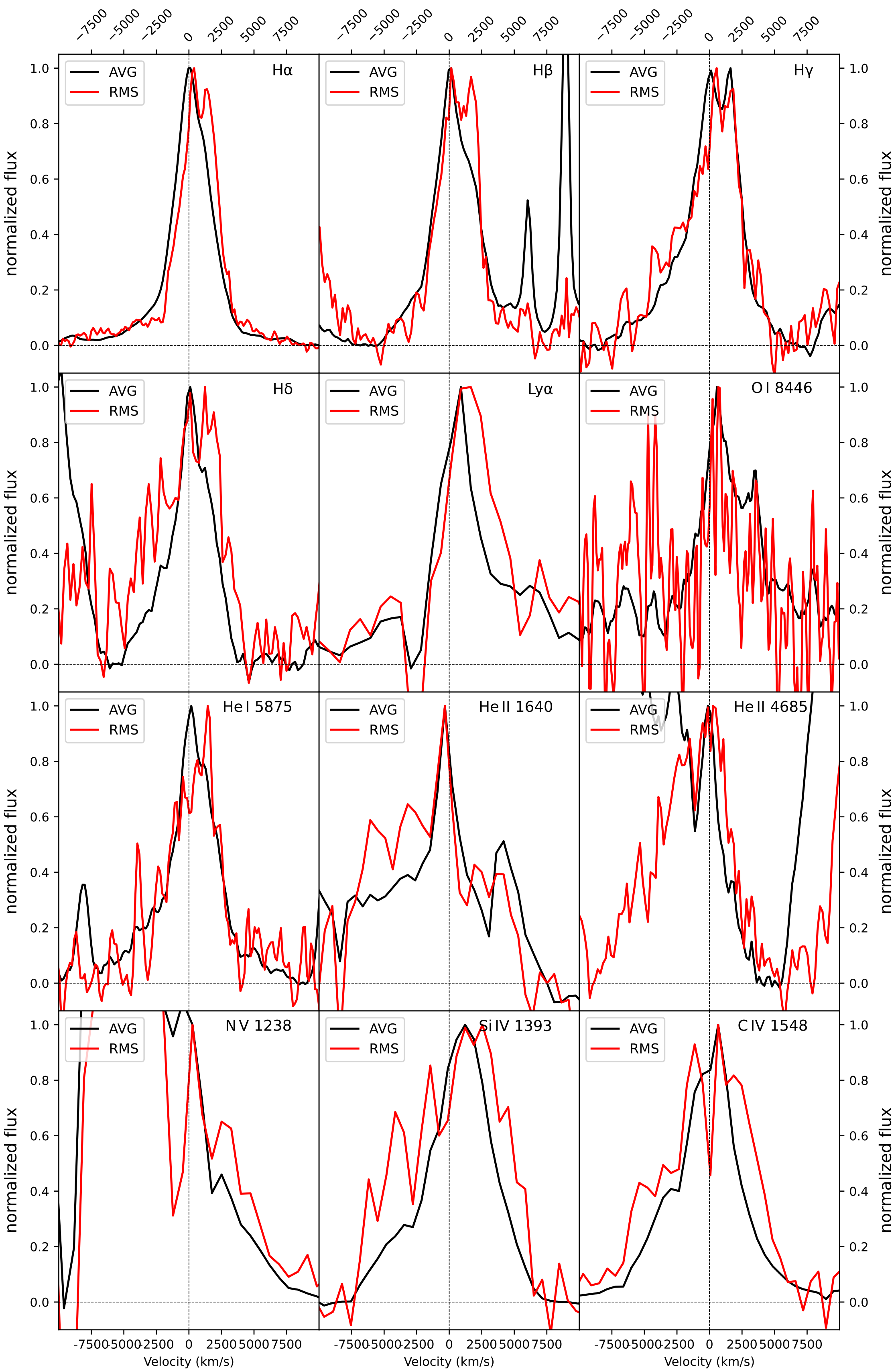

Figure 4.6: A plot of the AVG and RMS line profiles.

4.4.1 FWHM

After selecting the suitable broad emission lines, the FWHM of the normalized AVG and RMS profiles are calculated, which are listed in Table 4.6. Here the height of the line profile is defined between the zero-flux baseline and the maximum of the profile. The FWHM of the AVG profile of He II λ4685 was not attempted to be calculated, as the blue wing is mostly overlapped by the Fe II band between 4489 Å and 4629 Å. The uncertainties are estimated based on the instrumental dispersion of the grating, the shape and noise of the line profiles (see Table 3.1 for the gratings). Hα and He I λ5875 are measured with the G750L grating with a dispersion of 4.97 (Å/pixel), while the G430L grating has been use for Hβ, Hγ, and He II λ4685 with a dispersion of 2.73 (Å/pixel). By using Equation 4.7 and the rest-frame central wavelengths of the emission lines, this corresponds to an equivalent dispersion listed in Table 4.5. Taking the dispersion of the grating, the shape and the noise within the profiles, the uncertainties get estimated accordingly.

N kann ich die rechte flake nehmen und mit 2 multipliieren, da die linke flanke mit lyalpha überlagert ist. Lyalpha höhere fehler annehmen. Si raus nehmen, da eine abschetzung wegen der duplet überlagerung schwierig ist. HeII rechte seite abschätzen und mal 2, nur wenn es mit der anderen He II linie übereinstimmt einigermaßen. CIV sieht gut aus.

Table 4.5: Dispersion of grating in velocity space.

Line	**Dispersion** [$\frac{\text{km}}{\text{s}}$/pixel]
Hα	222.9
Hβ	169.3
Hγ	189.6
Hδ	200.6
He I λ5875	249.0
He II λ4685	175.6
Lyα	144.0
SiIV $\lambda\lambda$1393, 1402	125.6
CIV $\lambda\lambda$1548, 1550	113.1
HeII λ1640	106.7

4.4.2 Balmer-Lines

A comparison of the Balmer-line profiles Hα, Hβ, Hγ and Hδ are shown in Figure 4.8 With the exception of the AVG profile of Hγ, which is affected by the narrow [O III] λ4363 line overlapping the Hγ profile, the lines exhibit a similar asymmetric shape their AVG profiles. All three lines show a steep blue wing, that broads to a very

Table 4.6: Measured FWHM and of the AVG and RMS line profiles.

Line	**FWHM AVG[km/s]**	**FWHM RMS[km/s]**
Hα	2974 ± 250	3111 ± 250
Hβ	3439 ± 200	3437 ± 200
Hγ	4067 ± 200	3852 ± 300
Hδ	3398 ± 210	5905 ± 300
He I λ5875	3477 ± 300	3952 ± 300
He II λ4685	-	5971 ± 300
Lyα	3819 ± 150	4566 ± 150
SiIV $\lambda\lambda$1393, 1402	5330 ± 150	10005 ± 300
CIV $\lambda\lambda$1548, 1550	5413 ± 200	8428 ± 300
HeII λ1640	2847 ± 200	7459 ± 200

broad flank at about $\approx -2500\,\mathrm{km\,s^{-1}}$. H$\alpha$ and Hβ exhibit nearly identical gradients, while Hγ and Hδ shows a more broad flank up to $\approx -2500\,\mathrm{km\,s^{-1}}$ before matching the slope of the other profiles, which could be explained underlying components of other broad and narrow emission lines. The red wings of Hα and Hβ follow a similar pattern, showing a bump at around $\approx 1000\,\mathrm{km\,s^{-1}}$ and $\approx 2500\,\mathrm{km\,s^{-1}}$, respectively, resulting in the asymmetric profile and therefore velocity distribution. Looking at the line widths of the AVG profiles, the FWHM differs significantly from each other as the profiles consists of broad and narrow components and in case of Hγ is overlapped by the [O III] λ4363 emission line. These narrow components are hard to isolate in the profiles, no attempt was made to decompose the AVG profiles. The RMS profiles of the Balmer lines show an asymmetric double-peaked shape. Again, the profiles of Hα and Hβ show a very similar shape, while the blue wing of Hγ is more extended and becomes noisy towards increasing negative velocities, resulting in a higher line width compared to Hα and Hβ. Since [O III] λ4363 vanish in the RMS profiles, the red wing of Hγ becomes clearly visible and follows a similar shape of Hα and Hβ. For all three profiles, the double-peaked structure is red-shifted, with the blue peak located at $\approx 200\,\mathrm{km\,s^{-1}}$ and the red peak at $\approx 2000\,\mathrm{km\,s^{-1}}$, showing that most of the flux variation within the red wing of the emission lines.
Taking the strong similarities of the RMS profiles, it can be assumed that Hα, Hβ and Hγ emerge under similar kinematic properties.

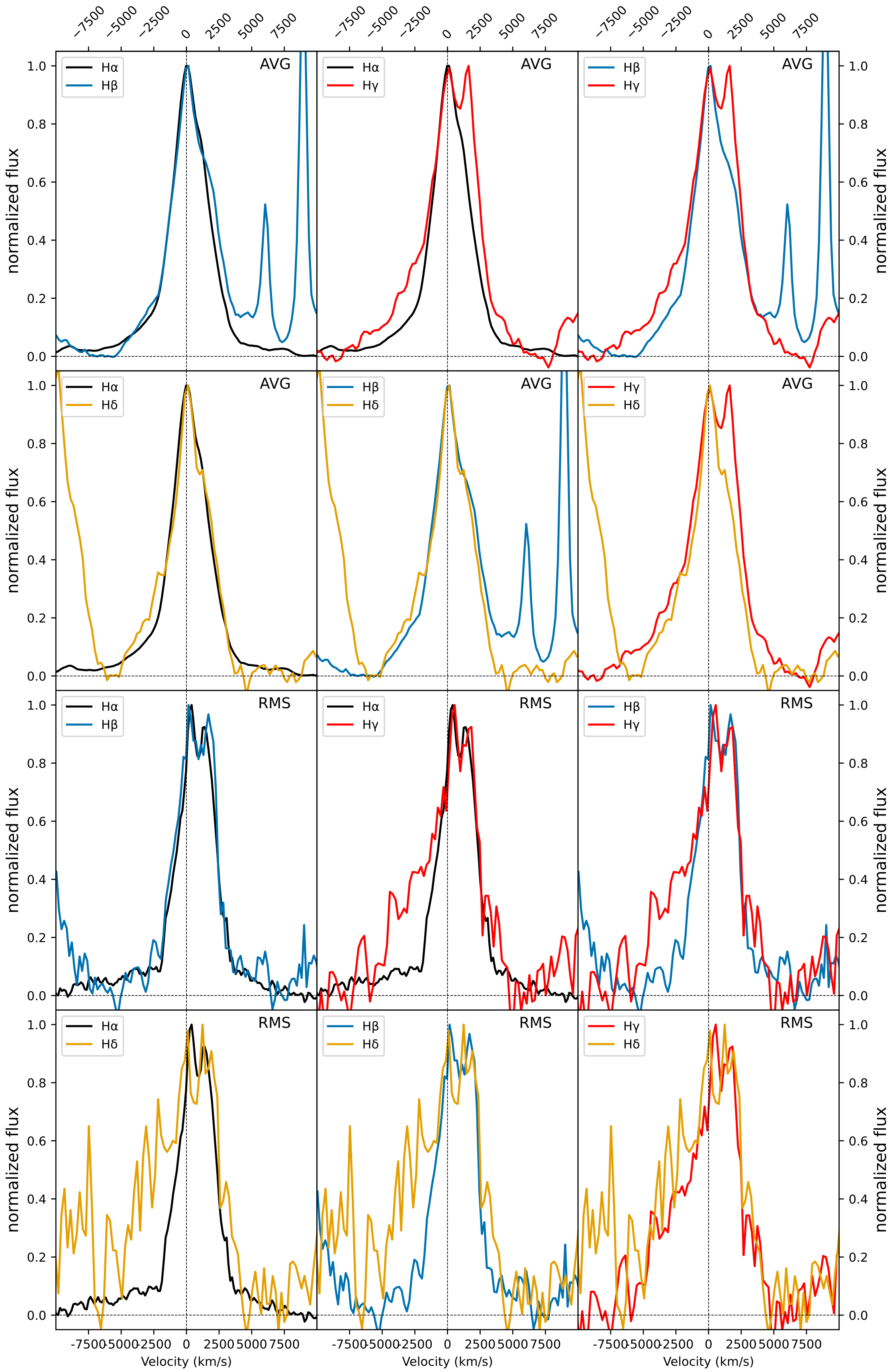

Figure 4.7: Comparison of the normalized AVG line profiles of the Balmer lines Hα, Hβ, Hγ and Hδ in velocity space.

4.4.3 Helium-Lines

Figure **??** shows a comparison of the AVG and RMS line profile of He I $\lambda5875$ and He II $\lambda4685$. The blue wing of the He II $\lambda4685$ AVG profile is partly overlapped by the Fe II band between 4489 Å and 4629 Å at velocities above about $-1000\,\mathrm{km\,s^{-1}}$. While the visible part of its blue wing follows the same shape as the He I $\lambda5875$ blue wing shape, the red wing of He I $\lambda5875$ is much broader. Still, both red wings show a similar shape and an additional smaller peak at around $1000\,\mathrm{km\,s^{-1}}$. Since more than half of He I $\lambda5875$ blue wing is overlapped by the Fe II band, a calculation of its FWHM was not attempted. Still, looking at the the line widths at 0.6 height of the line with $\approx 2500\,\mathrm{km\,s^{-1}}$ for He I $\lambda5875$ and $\approx 1600\,\mathrm{km\,s^{-1}}$ for He II $\lambda4685$ with using the uncertainties from Table 4.6, it can be assumed that He I $\lambda5875$ show a much broader FWHM in the AVG than He II $\lambda4685$. For the same reasons as for the balmer lines, a decomposition of the narrow and broad components was not attempted, which is why the FWHM of the RMS profiles will be used for the subsequent analysis.

Other than in the AVG profile, He I $\lambda5875$ now shows a smaller line width than He II $\lambda4685$ and higher noise. Looking at the He I $\lambda5875$ profile, its maximum is red-shifted to $\approx 2000\,\mathrm{km\,s^{-1}}$, while the maximum of the He II $\lambda4685$ profile is located around $0\,\mathrm{km\,s^{-1}}$. Following that it He I $\lambda5875$ shows more variation in its red wing than He II $\lambda4685$ does. The blue wing of He I $\lambda5875$ extend up to about $\approx -5000\,\mathrm{km\,s^{-1}}$ and its red wing about $\approx 4000\,\mathrm{km\,s^{-1}}$ while He II $\lambda4685$ blue wing extend up to about $\approx -9000\,\mathrm{km\,s^{-1}}$ its red wing about $\approx 5000\,\mathrm{km\,s^{-1}}$. Going from the maxima, it shows that both profiles show a much more extended blue wing and a very steep red wing.

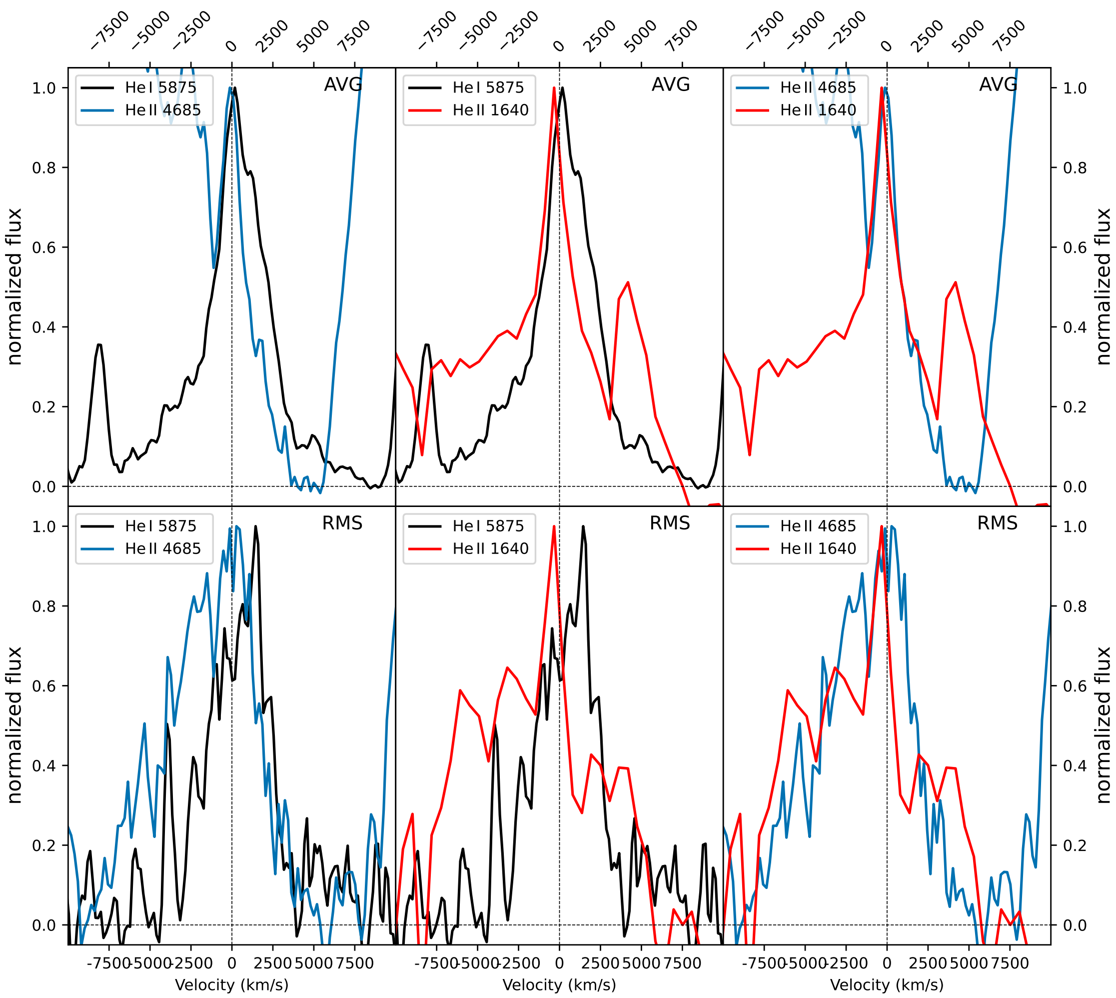

Figure 4.8: Comparison of the AVG and RMS line profiles of the Helium lines HeI $\lambda5875$ vs HeII $\lambda4685$.

4.5 Time Lag

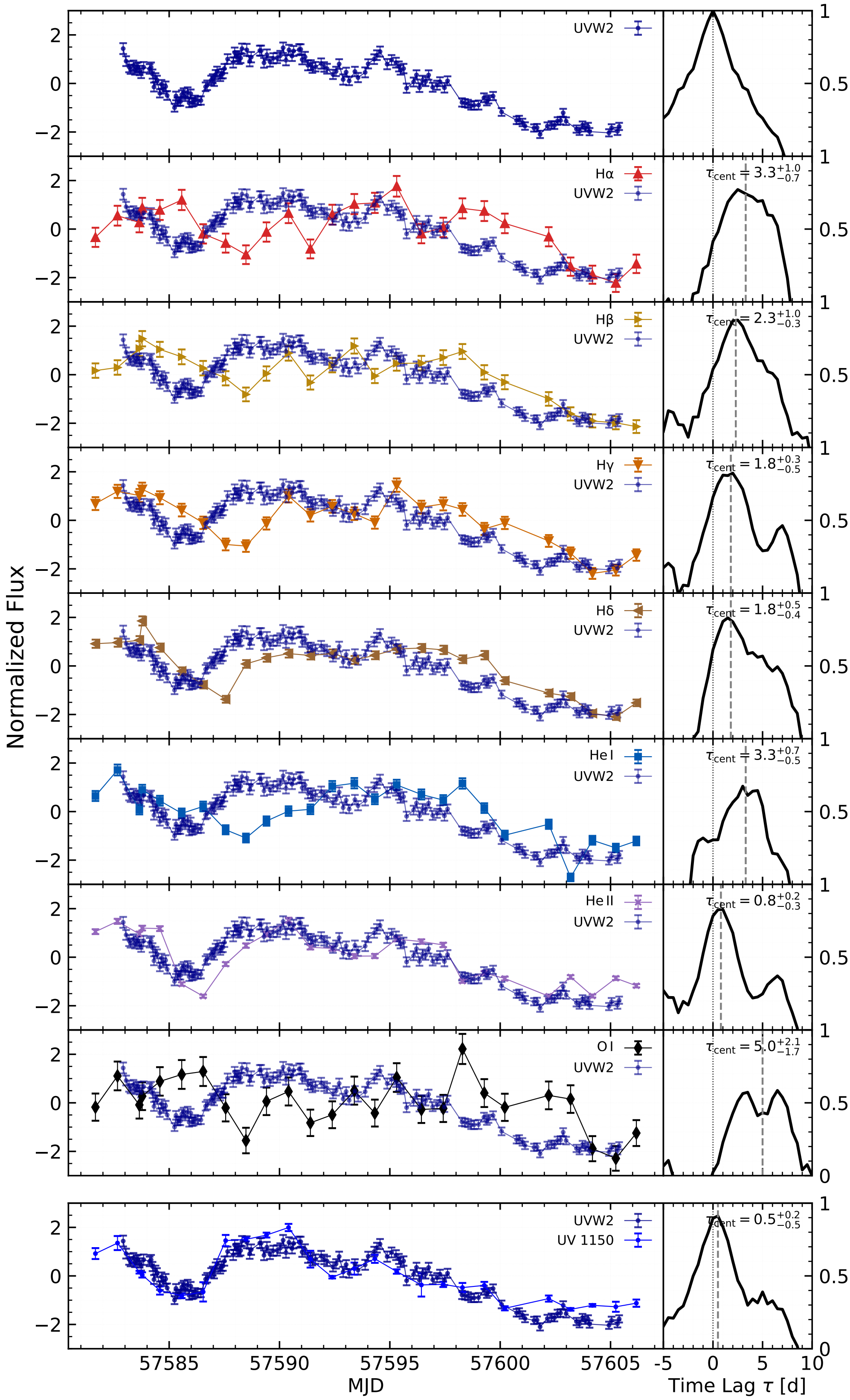

Figure 4.9: Compared lightcurves and CCFs Hα, Hβ, Hγ, He I λ5875, He II λ4685 and O I λ8446 with UVW2 as reference lightcurve.

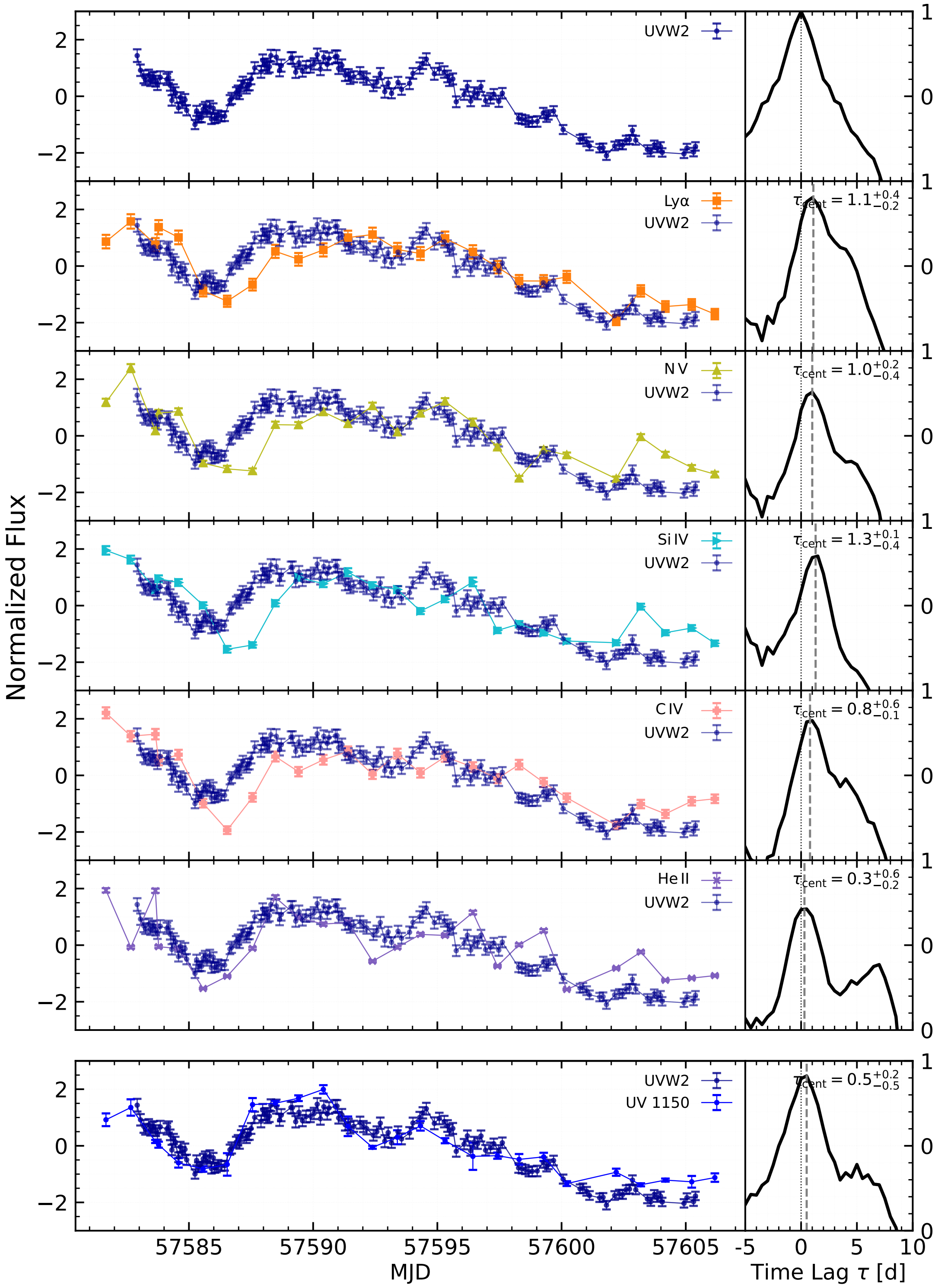

Figure 4.10: Compared lightcurves and CCFs of UV lines with UVW2 as reference lightcurve.

Table 4.7: Centroid and Peak Time Lag for UVW2.

Name	$\tau_{\rm cent}$ [d]
Lyα	$1.0^{+0.4}_{-0.2}$
Hα	$3.2^{+1.0}_{-0.6}$
Hβ	$2.3^{+1.0}_{-0.3}$
Hγ	$1.7^{+0.2}_{-0.4}$
Hδ	$1.7^{+0.4}_{-0.4}$
He I λ5875	$3.3^{+0.7}_{-0.4}$
He II λ1640	$0.3^{+0.6}_{-0.2}$
He II λ4685	$0.7^{+0.1}_{-0.3}$
O I λ8446	$5.0^{+2.1}_{-1.7}$
Si IV $\lambda\lambda$1393, 1402	$1.2^{+0.1}_{-0.4}$
C IV $\lambda\lambda$1548, 1550	$0.8^{+0.5}_{-0.0}$

4.6 Bowen Fluorescence of O I λ8446

Emission lines in the optical range, like the Balmer and helium lines, are commonly used in many reverberation-mapping campaigns, as they are easily accessible for nearby AGN (Ochmann et al. 2026). Other lines, such as the low-ionization line O I λ8446, have not been of major interest in such campaigns, mostly because of observational limitations (Ochmann et al. 2026). This is why the variability of the O I λ8446 line in this campaign is of particular interest, as the line can be enhanced by Bowen fluorescence, pumped by Lyβ emission (Grandi 1980). The time delay between the ionizing continuum and O I λ8446 should be consistent with a time delay in which continuum variations drive Lyβ variations, which in turn drive part of the O I λ8446 response. Unfortunately, Lyβ lies outside the spectral range of the Cackett et al. 2018 campaign. However, because the Lyα and Lyβ lines are expected to originate under similar physical conditions (Ochmann et al. 2026), Lyα can be used as a proxy for Lyβ. Hα is used to investigate the location of the O I λ8446 emitting region relative to the Balmer-line emitting region.

Therefore, the time lags between the UVW2 and emission-line lightcurves, as well as the CCFs and time lags between O I, λ8446 and Lyα, between Hα and Lyα, and between O,I λ8446 and Hα, are calculated and shown in Figure 4.11. All lightcurve show a strong correlation between $\approx 0.75 - 0.8$, with the exception of the O I λ8446 and UVW2 lightcurves, which show a maximum correlation of only 0.6. The time lags and their uncertainties are calculated as before. O I, λ8446 lags behind Lyα by $2.5{-}0.4^{+1.8}$ days and behind UVW2 by $5.0{-}1.7^{+2.1}$ days, while Hα lags behind Lyα by $1.8{-}0.5^{+0.5}$ days and behind UVW2 by $3.3{-}0.7^{+1.0}$ days. A difference in the response time of about 0.5–1 days between O I $\lambda8446$ and Hα is noticeable, but are not significant within the uncertainties. Looking at the O I $\lambda8446$ and Hα lightcurves, they also show a strong correlation, with O I $\lambda8446$ lagging behind Hα by about $0.3^{+2.0}_{-0.1}$ days. With the Lyα light curve lagging behind the UVW2 light curve by $1.1^{+0.4}_{-0.2}$ days, the total lag along the Bowen-fluorescence path from UVW2 to Lyα and from Lyα to O I $\lambda8446$ sums to ≈ 3.6 days, which lies within the uncertainties of the time lag between the Hα and UVW2 light curves.

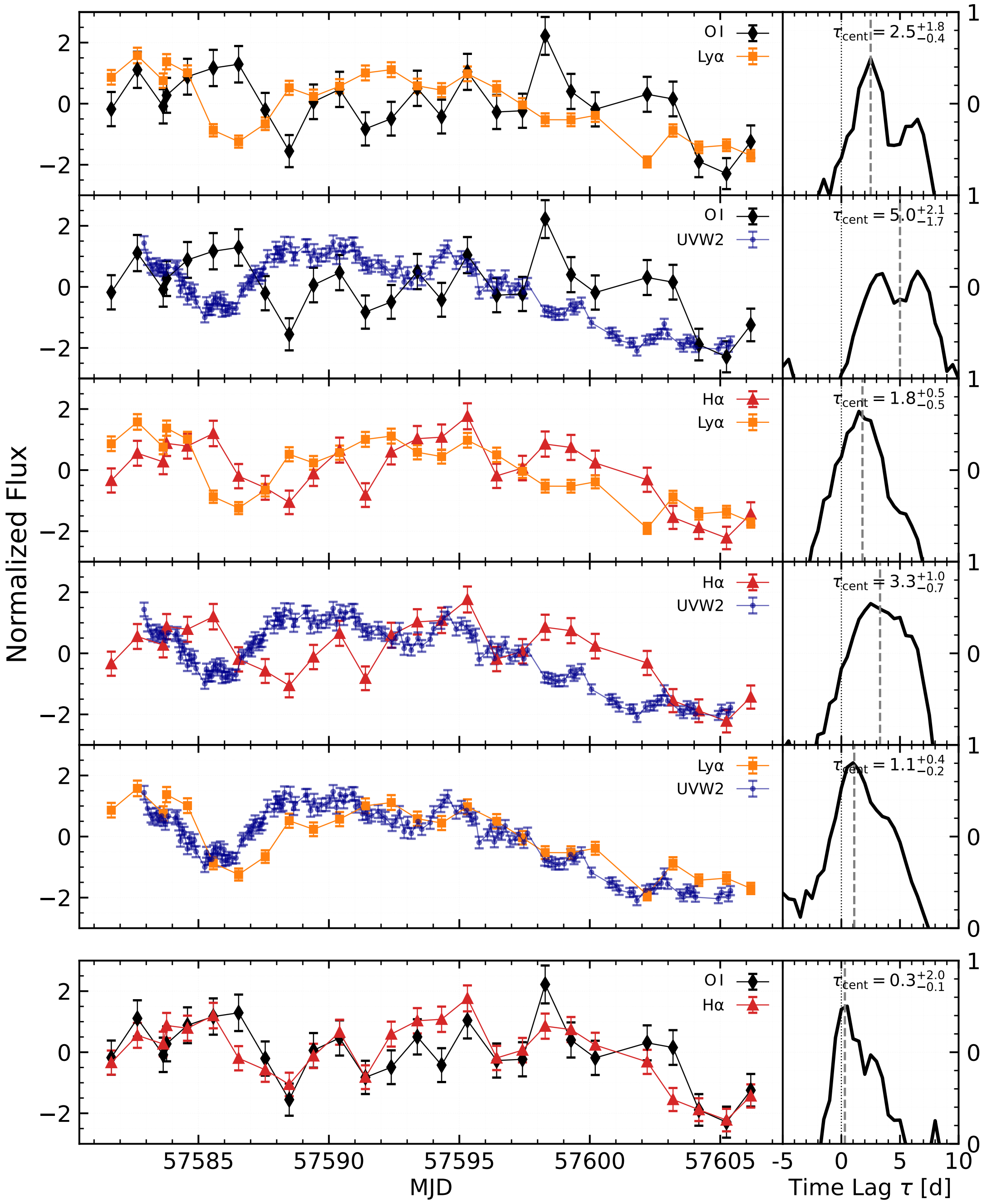

Figure 4.11: Compared lightcurves and CCFs for Bowen Fluorescence.

4.7 Black Hole Mass

Having obtained the time lags as well as the line widths of the selected broad emission lines, the mass of the SMBH can now be estimated using the virial theorem following the method of Peterson et al. 2004. Taking equation 2.7, 2.8 and 2.9 the SMBH mass can be estimated for each of the selected emission lines:

$$M_{\mathrm{BH}} = f \cdot \frac{c \cdot \tau_{\mathrm{centroid}}\, \Delta V^2}{G} \,. \tag{4.8}$$

The parameters are defined like described in section 2.2.3. The velocity dispersion ΔV^2 is parameterized by the line width of the emission line profile, which is measured using the FWHM of the RMS line profile. Following Probst et al. 2025 a scale factor of $f = 1.8$ gets assumed, that accounts the relation FWHM/$\sigma_{\mathrm{line}} \approx 2$ (Peterson et al. 2004). The resulting SMBH mass results, as well as the corresponding time lag and FWHM values of the broad emission lines are listed in Table 4.8.
To estimate a mean value of the BH mass, the inverse-variance weighted mean is calculated. Since the uncertainties are asymmetric a symmetrized 1σ uncertainty for the weights gets adopter, $\sigma_i = (\sigma_i^- + \sigma_i^+)/2$. The weighted mean is then given by

$$\bar{M}_{\mathrm{BH}} = \frac{\sum_i w_i M_{\mathrm{BH},i}}{\sum_i w_i} \,, \qquad w_i = \frac{1}{\sigma_i^2} \,, \tag{4.9}$$

with an uncertainty

$$\sigma_{\bar{M}} = \left(\sum_i w_i \right)^{-1/2} \,. \tag{4.10}$$

This yields the weighted-mean SMBH mass of $\bar{M}_{\mathrm{BH}} \approx (0.975 \pm 0.131) \times 10^7\, M_\odot$.
It has to be noted, that the scale factor of $f = 1.8$ does not account the low-inclination $i \sim 11°$ of the elliptic accretion disk, modeled in Ochmann et al. 2024. Adopting the scaling relation $f \sim \sin^{-2}(i)$ introduced by Krolik 2001, a value of $f \sim 27.5$ would be needed to account for the low inclination. Krolik 2001 used the line dispersion to parameterize the velocity dispersion, which is why the relation $\sigma_{\mathrm{line}} \approx$ FWHM/2 (Peterson et al. 2004) has to be accounted again. Due to the square relation of the velocity dispersion to the black hole mass seen in Equation 4.8, the scale factor finally gets corrected to a value $f \sim 6.8$. Subsequently the found BH mass has to be multiplied by a additional factor of 3.77.
Subsequently, the weighted-mean SMBH mass yields $\bar{M}_{\mathrm{BH,corr}} \approx (3.68 \pm 0.49) \times 10^7\, M_\odot$.

Table 4.8: Estimated time lags, FWHM and SMBH masses.

Name	$\tau_{\rm cent}$ [d]	FWHM (rms)[km/s]	$M_{\rm BH}[10^7 M_\odot]$
Lyα	$1.0^{+0.4}_{-0.2}$	4566 ± 150	$0.7^{+0.3}_{-0.2}$
Hα	$3.2^{+1.0}_{-0.6}$	3111 ± 250	$1.1^{+0.6}_{-0.4}$
Hβ	$2.3^{+1.0}_{-0.3}$	3437 ± 200	$0.9^{+0.6}_{-0.2}$
Hγ	$1.7^{+0.2}_{-0.4}$	3852 ± 300	$0.9^{+0.3}_{-0.3}$
Hδ	$1.7^{+0.4}_{-0.4}$	5905 ± 300	$1.5^{+0.6}_{-0.4}$
He I λ5876	$3.3^{+0.7}_{-0.4}$	3952 ± 300	$1.8^{+0.7}_{-0.5}$
He II λ1640	$0.3^{+0.6}_{-0.2}$	7459 ± 200	$0.5^{+1.2}_{-0.3}$
He II λ4686	$0.7^{+0.1}_{-0.3}$	5972 ± 300	$0.9^{+0.2}_{-0.4}$
C IV $\lambda\lambda$1548, 1550	$0.8^{+0.5}_{-0.1}$	8428 ± 300	$1.9^{+1.7}_{-0.2}$

5. Discussion

Bibliography

Aladin Lite (2025). CDS (Centre de Données astronomiques de Strasbourg). URL: https://aladin.cds.unistra.fr/AladinLite/ (visited on 07/19/2025).

Anderson, J. & L. R. Bedin 2010, *Publications of the Astronomical Society of the Pacific*, 122, 1035.

Antonucci, Robert 1993, *Annual Review of Astronomy and Astrophysics*, 31, 473–521.

Beckmann, Volker & Chris R. Shrader 2013, *The AGN phenomenon: open issues*, URL: https://arxiv.org/abs/1302.1397.

Bowen, I. S. 1934, *Publications of the Astronomical Society of the Pacific*, 46, 146–148.

Bowen, I. S. 1947, *Publications of the Astronomical Society of the Pacific*, 59, 196.

Cackett, E. M., M. C. Bentz, & E. Kara 2021, *iScience*, 24, 102557.

Cackett, E. M., C.-Y. Chiang, I. McHardy, et al. 2018, *The Astrophysical Journal*, 857, 53.

Denney, K. D., M. C. Bentz, B. M. Peterson, et al. 2006, *Astrophysical Journal Letters*, 653, 152–158.

Dexter, J. & E. Agol 2010, *The Astrophysical Journal*, 727, L24.

Gaskell, C. M. & B. M. Peterson 1987, *The Astrophysical Journal Supplement Series*, 65, 1.

Goad, M. R., K. T. Korista, & A. J. Ruff 2012, *Monthly Notices of the Royal Astronomical Society*, 426, 3086–3111.

Graham, A. W., C. A. Onken, E. Athanassoula, et al. 2011, *Monthly Notices of the Royal Astronomical Society*, 412, 2211–2228.

Grandi, S. A. 1980, *The Astrophysical Journal*, 238, 10.

Grier, C. J., P. Martini, L. C. Watson, et al. 2013, *The Astrophysical Journal*, 773, 90.

Horne, K., B. M. Peterson, S. J. Collier, et al. 2004, *Publications of the Astronomical Society of the Pacific*, 116, 465.

Hubble Advanced Spectral Products (HASP) (2025). Space Telescope Science Institute. URL: `https://archive.stsci.edu/missions-and-data/hst/hasp` (visited on 09/17/2024).

Institute, Space Telescope Science (2025). *STIS Instrument Handbook: Gratings*. URL: `https://hst-docs.stsci.edu/stisihb/chapter-13-spectroscopic-reference-material/13-3-gratings` (visited on 05/12/2025).

Keel, Bill (2002). *Quasars and Active Galactic Nuclei - Optical spectra of various kinds of active galactic nuclei*. Accessed: 2025-12-22. URL: `https://pages.astronomy.ua.edu/keel/agn/spectra.html`.

Kollatschny, W. & M. Dietrich 1997, *Astronomy and Astrophysics*, 323, 5–13.

Koss, M. J., C. Ricci, B. Trakhtenbrot, et al. 2022, *The Astrophysical Journal Supplement Series*, 261, 2.

Krolik, Julian H 2001, *The Astrophysical Journal*, 551, 72.

McHardy, I. M., S. D. Connolly, B. M. Peterson, et al. 2017, *Monthly Notices of the Royal Astronomical Society*, 465, 273–289.

McHardy, IM, SD Connolly, K Horne, et al. 2018, *Monthly Notices of the Royal Astronomical Society*, 480, 2881–2897.

Mikulski Archive for Space Telescopes (MAST) (2025). Space Telescope Science Institute. URL: `https://mast.stsci.edu/search/ui/#/hst` (visited on 09/17/2024).

Mo, H., F. van den Bosch, & S. White 2010, *Galaxy Formation and Evolution*, Cambridge University Press.

Netzer, H. 2013, *The Physics and Evolution of Active Galactic Nuclei*, Cambridge University Press, Cambridge.

Netzer, H. & M. V. Penston 1976, *Monthly Notices of the Royal Astronomical Society*, 174, 319–325.

Ochmann, M. W., W. Kollatschny, M. A. Probst, et al. 2024, *Astronomy & Astrophysics*, 686, A17.

Ochmann, M. W., P. M. Weilbacher, M. A. Probst, et al. 2025, *Astronomy & Astrophysics*, 697, L5.

Ochmann, Martin W, Edward M Cackett, Lukas Diehl, et al. 2026, *Astronomy and Astrophysics*, 705, L11.

Onken, C. A., L. Ferrarese, D. Merritt, et al. 2004, *The Astrophysical Journal*, 615, 645–651.

Osterbrock, D. E. 1977, *The Astrophysical Journal*, 215, 733–745.

Osterbrock, D. E. 1981, *The Astrophysical Journal*, 249, 462–470.

Osterbrock, Donald E. & Richard W. Pogge 1985, *The Astrophysical Journal*, 297, 166–176.

Peterson, B. M. 1993, *Publications of the Astronomical Society of the Pacific*, 105, 247–268.

Peterson, B. M. 1997, *An Introduction to Active Galactic Nuclei*, Cambridge University Press.

Peterson, B. M., L. Ferrarese, K. M. Gilbert, et al. 2004, *The Astrophysical Journal*, 613, 682–699.

Peterson, B. M. & K. Horne 2004, *Astronomische Nachrichten*, 325, 248–251.

Peterson, B. M., I. Wanders, K. Horne, et al. 1998, *Publications of the Astronomical Society of the Pacific*, 110, 660.

Peterson, Bradley M. 2011, *Masses of Black Holes in Active Galactic Nuclei: Implications for NLS1s*, URL: `https://arxiv.org/abs/1109.4181`.

Probst, M. A., W. Kollatschny, M. W. Ochmann, et al. 2025, *Emission-Line and Continuum Reverberation Mapping of the NLS1 Galaxy WPVS 48*, URL: `https://arxiv.org/abs/2511.09153`.

Rees, M. J. 1984, *Annual Review of Astronomy and Astrophysics*, 22, 471–506.

Ricci, C. & B. Trakhtenbrot 2023, *Nature Astronomy*, 7, 1282–1294.

Rodriguez-Pascual, PM, D Alloin, J Clavel, et al. 1997, *The Astrophysical Journal Supplement Series*, 110, 9.

Seyfert, Carl K. 1943, *The Astrophysical Journal*, 97, 28–40.

Shakura, N. I. & R. A. Sunyaev 1973, *Astronomy and Astrophysics*, 24, 337–355.

STScI (2025). *Digitized Sky Survey.* IPAC. DOI: `10.26131/IRSA441`. URL: `https://www.ipac.caltech.edu/doi/irsa/10.26131/IRSA441` (visited on 07/19/2025).

Ulrich, M.-H., L. Maraschi, & C. M. Urry 1997, *Annual Review of Astronomy and Astrophysics*, 35, 445–502.

Urry, C. M. & P. Padovani 1995, *Publications of the Astronomical Society of the Pacific*, 107, 803–845.